ADAR1 haploinsufficiency and sustained picornaviral RdRp dsRNA synthesis synergize to dysregulate RNA editing and cause multi-system interferonopathy

Caitlin M. Miller[1,3], James H. Morrison[1,3], Laura Bankers[1], Rachael Dran[1], Julia M. Kendrick[1], Emma Briggs[2], Virginia L. Ferguson[2], and Eric M. Poeschla[1*]

[1]Division of Infectious Diseases, Anschutz Medical Campus, University of Colorado School of Medicine, Aurora, Colorado, USA 80045
[2]Department of Mechanical Engineering and BioFrontiers Institute, University of Colorado at Boulder, Boulder, CO, 80309
[3]These authors contributed equally
[*]Correspondence: eric.poeschla@cuanschutz.edu

ABSTRACT

Sensing of viral double-stranded RNA by MDA5 triggers abundant but transient interferon-stimulated gene (ISGs) expression. If dsRNA synthesis is made persistent by transgenically expressing a picornaviral RNA-dependent RNA polymerase (RdRp) in mice, lifelong MDA5-MAVS pathway activation and marked, global ISG upregulation result. This confers robust protection from viral diseases but in contrast to numerous other chronic MDA5 hyperactivation states, the mice suffer no autoimmune or other health consequences. Here we find they further confound expectations by being resistant to a strong autoimmunity (lupus) provocation. However, knockout of one allele of *Adar* breaks the autoinflammation-protected state of RdRp^{tg} mice and results in a severe disease that resembles interferonopathies caused by MDA5 gain-of-function protein mutations. *Adar*$^{+/-}$ mice are healthy but *Adar*$^{+/-}$ RdRp^{tg} mice have shortened lifespan, stunted growth, premature fur graying, poorly developed teeth, skeletal abnormalities, and extreme ISG elevations. A-to-I edits are both abnormally distributed and increased (numbers of genes and sites). These results, with a nucleic acid-triggered and MDA5-wild type model, illuminate the ADAR1-MDA5 axis in the regulation of innate immunity and establish that viral polymerase-sourced dsRNA can drive autoinflammatory disease pathogenesis.

Keywords: ADAR1; MDA5; innate antiviral immunity; picornavirus; RdRp; autoimmunity; autoinflammation; interferonopathy; lupus

37 **IMPORTANCE**

38

39 RNA virus double-stranded RNAs are important pathogen associated molecular patterns that are
40 sensed by the RIG-I like receptor MDA5, which triggers an acute innate immune response involving
41 many ISGs. One key to a healthy innate immune system is that MDA5 not sense endogenous
42 dsRNA. This is normally ensured by dsRNA duplex-disrupting ADAR1 editing of host dsRNAs.
43 Picornavirus RdRp^{tg} mice have an unusual constitutive MDA5 activation state, with very high lifelong
44 MDA5-mediated ISG expression that confers robust protection from diverse lethal viruses.
45 Importantly, and in contrast to numerous other chronic MDA5 hyperactivation states, the mice
46 develop no autoinflammatory consequences. If we delete one ADAR1 allele, however, which by itself
47 is well tolerated, the mice develop a multisystem disease that resembles the human interferonopathy
48 Singleton-Merten syndrome. In contrast to other MDA5/ADAR1 disease models, the MDA5 and
49 ADAR1 proteins are both wild type in this dsRNA-driven model.

50

51

52

53

INTRODUCTION

Double-stranded RNA (dsRNA), a requisite intermediate during the replication of RNA viruses, is a pathogen-associated molecular pattern that induces an array of first-line antiviral defenses. Two specialized RNA helicases function as the main pattern recognition receptors (PRRs) that detect viral dsRNA: retinoic acid inducible gene-I (RIG-I) and melanoma differentiation antigen 5 (MDA5). Both of these RIG-I-like receptors (RLRs) are cytosolic sensors that signal through the adaptor MAVS, which instigates signaling cascades that eventuate in expression of numerous ISGs, either directly or via induction of secreted type I interferons (IFN-I) (1). RIG-I in general detects shorter or 5'-ppp containing dsRNAs and MDA5 detects the internal segments of longer (> 1 to 2 kb) dsRNAs (2-4). A few RNA viruses are exclusively sensed by one RLR (1). Picornaviral dsRNAs, for example, are detected by MDA5 and not RIG-I (1, 5-8).

The challenge such a system poses for the host is to securely differentiate viral dsRNAs from the vast, diverse pool of cellular RNAs, many of which can also harbor extended RNA duplex segments, particularly within retroelement-derived RNAs that are abundant in mammalian genomes (9, 10). Inappropriate or sustained activations of RLRs and other signaling pathways by endogenous nucleic acid ligands are associated with a variety of autoimmune diseases, which include classical, common syndromes such as systemic lupus erythematosus (SLE), type I diabetes mellitus, and psoriasis as well as various and frequently severe genetic conditions known collectively as interferonopathies. These auto-inflammatory conditions are characterized by persistent IFN-I and ISG expression and diverse end organ pathologies (5, 11, 12).

The RNA modifying enzyme Adenosine Deaminase Acting on RNA 1 (ADAR1) has recently been identified as a central constraint on dsRNA-triggered autoimmunity (13-17). Encoded by *ADAR*, ADAR1 catalyzes post-transcriptional editing of host RNAs by deaminating adenosine to inosine, thereby disrupting A-U base-paring and preventing formation of long uninterrupted RNA duplexes (9, 10, 18, 19). A-to-I editing most prominently prevents detection by MDA5 or protein kinase regulated by dsRNA (PKR) of endogenous retroelement transcripts and other dsRNAs, which averts inappropriate immune activation or translational shutoff (9, 10). Such editing of transcripts can also cause protein recoding (17, 20, 21), although the vast majority of A-to-I edits in mammals are in non-coding regions (22-25). Strikingly, physiologically essential A-to-I editing represents a very small fraction of the editome, and moreover most editing is unnecessary for murine homeostasis in the absence of MDA5 (26, 27). Hereditary mutations in

88 *ADAR*, as well as in other genes such as *TREX1*, *SAMHD1*, *RNASEH2, RNU7, LSM11, and*
89 *IFIH1* (MDA5) have been linked to the development of the rare congenital inflammatory disorder
90 Aicardi-Goutières syndrome (AGS), which clinically mimics encephalopathies caused by *in*
91 *utero*-acquired virus infections (11, 14, 28-33). Homozygous *Adar* gene knockout is embryonic
92 lethal in mice, causing mass apoptosis of fetal liver hematopoietic cells by embryonic day 11.5-
93 12.5 (20, 34). In contrast, $Adar^{+/-}$ mice are phenotypically normal and born at expected
94 Mendelian ratios (18). Early fetal demise of $Adar^{-/-}$ mice has been linked mechanistically to
95 activation of the MDA5 pathway by dsRNA regions in cellular RNAs, chiefly repetitive elements,
96 that are normally masked by A-I editing (15, 18, 20, 34, 35).
97
98 Indeed, constitutive MDA5 activation has been repeatedly observed to cause autoimmune
99 syndromes such as AGS in both mice and humans (31, 36). In distinctive counterpoint, we have
100 shown in a mouse model that chronic, systemic MDA5 activation caused by viral polymerase-
101 generated dsRNA, which causes marked, lifelong ISG upregulation, can be well-tolerated, even
102 when it is also strongly protective against viral diseases (37-39). The mice are transgenic for the
103 RdRp of a neurovirulent mouse picornavirus (Theiler's murine encephalomyelitis virus, TMEV)
104 expressed under transcriptional control of the non-selective ubiquitin C promoter, which causes
105 chronic dsRNA-triggered innate immune activation (37, 38). Tissues of the RdRp transgenic
106 mice ($RdRp^{tg}$ mice; see first Methods section for nomenclature) express low levels of the
107 polymerase, which templates on host RNAs to synthesize dsRNA. Elevated dsRNA is detected
108 in $RdRp^{tg}$ mouse tissues using the K1 anti-dsRNA antibody (37). In addition, a catalytic center
109 mutant of the TMEV RdRp lacked all ISG up-regulating activity (37). $RdRp^{tg}$ mice have global,
110 high upregulations of ISGs and robust protection against ordinarily lethal challenges by a variety
111 of RNA and DNA viruses, including Theiler's virus itself, EMCV, vesicular stomatitis virus, a
112 DNA herpesvirus (pseudorabies virus), and Friend retrovirus (37, 38, 40, 41). The model is
113 mouse strain-independent, with equivalent phenotypes in FVB/NJ, BALB/c and C57BL/6J mice.
114
115 $RdRp^{tg/-}$ and $RdRp^{tg/tg}$ mice develop normally, with onset of the major ISG expression profile
116 shortly after birth (39). The intriguing lack of deleterious effects from their chronically elevated
117 ISGome differs strikingly from other constitutive MDA5 activation states (36). Body size,
118 morphology, organ histology and longevity are normal (37-39). Crosses with $Ifih1^{-/-}$ mice showed
119 that the sustained innate immune activation is strictly dependent on MDA5, which is congruent
120 with MDA5 but not RIG-I being the sensor of picornaviral dsRNAs (1, 5-8). It is further
121 dependent on the downstream adaptor MAVS, and the type I IFN receptor (IFNAR1) and is

122 abolished by knockout of these genes (37). Although type I IFNs are not detectably over-
123 expressed in RdRp^{tg} mice tissues, antibody-mediated blockade of the type I IFN receptor in
124 adults terminates the ISG profile, indicating that some ongoing IFN-I signaling is required to
125 sustain it (38, 39). *TLR3*, *IFNGR1* and *RAG1* knockout crosses also showed the ISG profile
126 does not depend on TLR3, interferon gamma signaling or the adaptive immune system. As
127 expected from the complete abrogation of ISG upregulation by *Ifih1* knockout, *Ddx58* knockout
128 mouse crosses further confirmed no dependence on RIG-I (our unpublished data). Thus, the
129 model is distinctive in that it represents a pure dsRNA-induced MDA5 hyperactivation state, and
130 also one that is mediated through the wild type MDA5 sensor, and via "viral" dsRNA.
131
132 Prompted by the well-tolerated ISG elevations in this model, we here carried out experiments
133 that demonstrate that RdRp^{tg} mice also resist induction of SLE in the BM12 lupus model, which
134 we find is linked to increased quantities and effector function of regulatory T cells (T_{reg}). We
135 show that introducing single *Adar* allele knockout – which, similar to RdRp transgenesis,
136 produces no abnormalities by itself – breaks the RdRp^{tg} protective state, yielding a severe
137 autoinflammatory disease. RdRp^{tg} mice lacking one *Adar* allele have stunted growth, gray fur,
138 abnormal dental and skeletal structures, failure to thrive, highly dysregulated ISG expression,
139 and abnormal A-to-I editing. This dsRNA-driven, MDA5-wild type model establishes that viral
140 polymerase-sourced dsRNA can drive interferonopathy pathogenesis and illuminates the
141 autoimmunity preventing role of ADAR1.
142
143
144 **RESULTS**
145
146 **RdRp^{tg} mice resist induction of SLE.** Since picornaviral RdRp^{tg} mice do not exhibit apparent
147 fitness "costs" of their chronic immune system activation (37-39), an unanswered question is
148 whether they may be more autoimmunity-prone like other constitutive MDA5 activation models
149 (36, 42, 43). To address this experimentally, we carried out a strong autoimmunity provocation
150 by adopting the BM12 inducible SLE model, in which lupus is initiated by injection of
151 splenocytes from MHC class II-mismatched mice (44, 45). Wild type (WT) and RdRp$^{tg/-}$ mice
152 were injected with $1x10^8$ splenocytes isolated from BM12 mice or were control-injected with
153 PBS and evaluated for disease two weeks later. One of the clearest morphological changes in
154 the BM12 model is splenomegaly, which results from germinal center expansion. Spleens were
155 harvested and weighed before processing for flow cytometric analyses. As anticipated, we

156 observed a significant increase in spleen size in WT mouse BM12 splenocyte recipients,
157 indicative of lupus-like disease initiation (**Fig. 1A**). In contrast, RdRp^{tg} mouse BM12 splenocyte
158 recipients had only minor, statistically non-significant increases in spleen size (**Fig. 1A**, p =
159 0.126 as compared with PBS-injected RdRp^{tg} mice).
160
161 We next examined cellular subsets in the spleen, specifically germinal center B cells and
162 plasma B cells, which expand as they become activated to secrete anti-nuclear antibodies
163 (ANAs), and T follicular helper (T_{fh}) cells, which provide antigenic stimulus in germinal center
164 reactions (46, 47). For all three cell populations, WT mouse BM12 splenocyte recipients
165 developed significant increases, indicative of ongoing germinal center reactions and increased
166 antibody production (**Fig. 1B,C**). In contrast, and paralleling the spleen measurements, RdRp^{tg}
167 mouse BM12 splenocyte recipients developed little to no increases in all three cellular
168 populations. Significant increases over sham-treated animals were only seen in germinal center
169 B cells (**Fig. 1B,C).** Minor changes in overall B cell and T cell populations were also observed,
170 but none that account for the drastic differences in cellular subsets seen in WT BM12
171 splenocyte recipient animals (**Fig. S1A,B**).
172
173 To corroborate the results, we collected serum from splenocyte-recipients and control PBS
174 recipients to measure production of ANAs, which are a hallmark of SLE and drive pathology in
175 this model (44, 45). We measured ANAs against double-stranded DNA (dsDNA) and Smith
176 antigen (SmAg), both of which are frequently observed in SLE patients and SLE mouse models
177 (47, 48) (**Fig. 1D**). Similar to the changes in cellular populations, there were significant
178 increases in both of these autoantibodies in WT BM12 splenocyte recipients compared to the
179 PBS recipient controls. In contrast, the RdRp^{tg} mouse BM12 splenocyte recipients produced
180 less of both autoantibodies.
181
182 **T_{reg} cell expansion**. Our previous investigations did not reveal significant differences in immune
183 cell subsets between WT and RdRp^{tg} mice (38). Here we extended the studies to assess
184 autoimmune suppressor cells, specifically regulatory T cells (T_{regs}), which are critical for
185 maintaining immune-tissue homeostasis. Knockout of T_{regs} results in disseminated autoimmune
186 disease followed by rapid organismal decline and death (49, 50). We measured T_{reg} cell subsets
187 in age-matched animals. There was a highly significant increase in T_{reg} cells in RdRp$^{tg/-}$ mice
188 compared to WT and specifically an increase in mature, effector T_{regs} (**Fig. 1E**). T_{reg} cell
189 expansion in RdRp^{tg} mice may aid their tolerance to chronic innate immune activation.

190

191 The combined cellular and ANA data indicate that RdRp^{tg} mice are better able to control
192 disease induction after an autoimmune provocation than WT mice. This result is distinctive
193 compared to other MDA5-pathway driven hyperimmune mice models, which have been shown
194 to be equally or more susceptible to autoimmunity induction (42, 43)
195

196 **Investigation of ADAR1.** In addition to Treg cells, we suspected that mechanisms of protection
197 at the intrinsic cellular level are likely to provide key regulation. Given its known role in
198 preventing activation of the MDA5 pathway by double stranded segments of endogenously
199 encoded RNAs, we hypothesized that ADAR1 may prevent adverse inflammatory sequelae in
200 RdRp^{tg} mice. First, we determined whether *Adar* expression is affected by RdRp genotype
201 status. *Adar* encodes two functional isoforms, ADAR1 p150, which edits transcripts in the
202 cytoplasm and is IFN-inducible, and constitutively expressed ADAR1 p110, which is generated
203 by alternative splicing or by translation from the p150 mRNA by leaky internal ribosome
204 scanning (51) and edits transcripts in the nucleus (19, 52, 53). We observed no significant
205 difference at either the mRNA or protein levels in expression of the p110 isoform in RdRp^{tg} mice
206 as compared to WT mice (**Fig. 2A,C**). In contrast, there was a marked increase in expression of
207 the IFN-inducible p150 isoform (**Fig. 2B,C).** These results suggested that ADAR1 p150, itself an
208 ISG, is upregulated in RdRp mice, perhaps helping to modulate the ISG activation in these
209 animals.
210

211 We next knocked down *ADAR* expression in human lung epithelial cells (A549) in which we
212 have engineered and validated inducible TMEV RdRp expression under the control of a
213 doxycycline (dox) inducible promoter (37). These cells broadly upregulate ISGs in response to
214 RdRp induction in a pattern very similar to the RdRp^{tg} mouse (37). In two separate experiments,
215 we achieved knockdowns of ADAR p110 and p150 isoforms (**Fig. 2D**). Dox induction of the
216 RdRp after siRNA transfection led to over three $\log_{10}$ increases in mRNAs for two classical
217 ISGs, *OAS* and *ISG15*, which were moderately accentuated by *ADAR* depletion in these short-
218 term experiments (**Fig. 2E**). We therefore proceeded to generate mice with *Adar* gene
219 knockouts.
220

221 ***Adar* haploinsufficiency, by itself well-tolerated, causes multi-system disease in RdRp^{tg}**
222 **mice.** As noted, by two weeks after birth, RdRp^{tg} mice develop high, sustained upregulations of
223 many ISGs and subsequently tolerate them throughout their (normal) lifespans (37, 39). To

224 determine whether ADAR1 is involved in the protection against deleterious effects of
225 autoinflammation, *RdRp*$^{tg/tg}$ mice were crossed with *Adar*$^{+/-}$ mice. *RdRp*$^{tg/-}$ mice also have
226 elevated ISGs, albeit with more variability in fold-induction than RdRp$^{tg/tg}$ mice (for example, see
227 **Fig. 2B,C** for expression of the ISG ADAR1 p150, and Painter et al. (37)). Since in our hands
228 and others *Adar*$^{+/-}$ mice have no phenotypic abnormalities, we did not anticipate a major effect in
229 first-generation crosses even in the presence of an RdRp-mediated ISG response, since the F1
230 animals will retain a functional *Adar* allele.
231
232 However, that was not the outcome. First, there were major gross phenotypic differences
233 between *RdRp*$^{tg/-}$ *Adar*$^{+/-}$ mice and littermate *RdRp*$^{tg/-}$ *Adar*$^{+/+}$ controls (**Fig. 3A-C**). The RdRp^{tg}
234 mice lacking one *Adar* allele were significantly smaller in size (**Fig. 3A, B**), with gray instead of
235 black fur (**Fig. 3A, C**). These features were equivalent in males and females (**Fig. 3A, C**).
236 *RdRp*$^{tg/-}$ *Adar*$^{+/-}$ mice also have small, poorly developed, misshapen teeth (**Fig. 3C**). Runting was
237 unrelated to the dental abnormalities, since suckling behavior was unaffected. In addition, the
238 size evaluations were done at the time of weaning, and post-weaning mice were kept on a wet
239 chow diet, which they were also observed to ingest equivalently. *Adar*$^{+/-}$ mice were normal in
240 appearance as expected.
241
242 Because of these phenotypic differences, we carried out tissue dissections. Survival of the
243 *RdRp*$^{tg/-}$*Adar*$^{+/-}$ mice began to fall significantly by 10 weeks after birth (**Fig. 3D**), so these studies
244 were done at 4-5 weeks. Soft viscera including heart, lungs, liver, spleen, intestines, kidney and
245 brain were proportionately small but the organ morphologies were otherwise not different from
246 WT mice. Histopathology analysis of tissue sections by a veterinary pathologist did not reveal
247 evidence for tissue inflammation or other abnormalities (**Fig. 3E;** see Supplemental Methods for
248 scoring and data). Since some MDA5-driven mouse autoimmune models manifest with kidney
249 impairment, blood urea nitrogen (BUN) values were determined at 4-5 weeks of age. Mean BUN
250 was slightly higher in RdRp^{tg} mice but was not in either *Adar*$^{+/-}$ group (**Fig. 3F**). We also
251 measured serum ANAs and found no significant increases in anti-dsDNA antibodies (data not
252 shown as levels for all animals were below the limit of assay detection) or anti-SmAg antibodies
253 (**Fig. 3G**). In addition to the abnormal teeth, necropsy revealed thin, pale long bones suggesting
254 decreased bone density. Bone frailty was also readily apparent during cervical dislocations,
255 which subjectively required much less force Similar dental and bone abnormalities can occur in
256 Singleton-Merten Syndrome (SMS), a rare human autosomal dominant innate immune disorder
257 consisting of musculoskeletal abnormalities (osteopenia, osteoporosis, skull thickening, small

258 stature, ligament frailty), dental anomalies (poor, primarily anterior teeth formation), variable
259 arterial calcification, inflammatory skin changes (psoriasis), and a characteristic facies (high
260 anterior hair line, broadened forehead, asymmetric ptosis, smooth philtrum, and thin upper
261 vermillion) (54, 55). Genetic studies of individuals with SMS have revealed causation by a
262 subset of single amino acid missense gain-of-function (GOF) mutations in MDA5 (R822Q,
263 A489T, T331I/R), which cause constitutive activation (56-60). There is inter-familial and intra-
264 familial variation in syndromic manifestations, with partial penetrance evident in some
265 kindreds(55). and overlap with Aicardi-Goutières syndrome has been reported (58, 59, 61).
266 Similarly, two families with atypical SMS lacking the dental abnormalities were found to have
267 constitutively active single amino acid mutants of RIG-I rather than MDA5 (62).
268
269 As *RdRp*$^{tg/-}$ *Adar*$^{+/-}$ mice had micrognathia as well as small, misshapen and partially translucent
270 incisors (**Fig. 3C**), µCT imaging and mechanical property assessments of femurs were
271 performed to determine whether *RdRp*$^{tg/-}$ *Adar*$^{+/-}$ mice also had altered underlying changes to
272 bone architecture or properties. Consistent with the runting observed in 5-week-old mice (**Fig.
273 3A,B**), femurs of 6-week-old *RdRp*$^{tg/-}$ *Adar*$^{+/-}$ were significantly shorter than control groups (**Fig.
274 4A,B**). As in other RLR-related genetic disorders (55, 62), weight, femur length, and other
275 mouse characteristics were variably penetrant. Bartlett's test demonstrated a statistically
276 significant (p=0.0142) difference in homoscedasticity for femur length, yet a Kolmogorov-
277 Smirnov test did not identify significant (alpha=0.05) deviation from normal distribution for
278 *RdRp*$^{tg/-}$ *Adar*$^{+/-}$ or other groups. Thus, we did not separate *RdRp*$^{tg/-}$ *Adar*$^{+/-}$ mice into 'penetrant'
279 and 'non-penetrant' subsets in subsequent analyses and graphics, but we labeled mice with
280 gray fur with light blue symbols in Fig. 4. *RdRp*$^{tg/-}$ *Adar*$^{+/-}$ femurs had significantly reduced
281 cortical bone volume fraction and correspondingly reduced measures of cortical thickness,
282 perimeter, area and porosity (**Fig. 4C**). In contrast, trabecular number and trabecular separation
283 were not different between groups (**Fig. 4D-E**). Mechanical properties of the femurs were further
284 investigated using three-point bending to failure. Stiffness and maximum load of *RdRp*$^{tg/-}$ *Adar*$^{+/-}$
285 femurs were significantly reduced compared to control groups (**Fig. 4F,G**). Modulus and
286 ultimate stress of the femurs were calculated from mechanical properties and mid-diaphysis
287 cross-sectional geometry from µCT. In contrast to the reduced mechanical properties observed,
288 these material properties of *RdRp*$^{tg/-}$ *Adar*$^{+/-}$ femurs were not altered (**Fig. 4I-J**), nor was the total
289 cortical mineral density calculated from the µCT imaging (**Fig. 4H**). These results indicate that
290 double heterozygosity (*RdRp*$^{tg/-}$ *Adar*$^{+/-}$) led to femurs having inferior stiffness and strength

291 stemming from smaller size but not from impaired bone material quality, in addition to their
292 dental maldevelopment and fur graying.
293
294 Resemblance to classical human SMS was partial since we the mice did not develop aortic or
295 cardiac valvular calcification, a core feature of the human syndrome, nor was there aberrant
296 brain calcification (**Fig. S2**) as occurs in AGS (11) and in some SMS-AGS overlap cases(58, 59,
297 61). Psoriasis is less commonly observed in SMS patients and was not observed in *RdRp*$^{tg/-}$
298 *Adar*$^{+/-}$ animals, leaving fur graying as the identifiable integument abnormality. Glaucoma can
299 also occur in SMS, but intraocular pressures measured by tonometry in affected mice were
300 normal and not significantly different from WT mice (data not shown).
301
302 **Transcriptional changes in *RdRp*$^{tg/-}$ *Adar*$^{+/-}$ mice are consistent with an interferonopathy.**
303 The SMS-resembling phenotype triggered by the combination of one RdRp transgene allele and
304 one *Adar* null allele, with neither alone producing abnormalities, prompted us to examine tissues
305 further for differences that may be driving pathogenesis. We performed RNA-seq on brain
306 tissue, with four biological replicates from each of the four genotypes WT, *Adar*$^{+/-}$, *RdRp*$^{tg/-}$ and
307 *RdRp*$^{tg/-}$ *Adar*$^{+/-}$. Brains were analyzed because we previously observed that brains of RdRp^{tg}
308 mice have particularly high ISG elevations compared to other organs, although gene expression
309 changes are qualitatively similar and substantial across all major organs (39). Here, in
310 multidimensional scaling plots, we observed that the samples cluster strongly by genotype along
311 the M1 axis, which validates that animals of the same genotype have similar gene expression
312 profiles (**Fig. 5A**). The double heterozygotes (*RdRp*$^{tg/-}$ *Adar*$^{+/-}$) cluster the farthest from any other
313 genotype, suggesting they have distinctly different RNA expression patterns. Assessing
314 expression changes across the groups, the greatest differences were between *RdRp*$^{tg/-}$ *Adar*$^{+/-}$
315 mice relative to WT mice and relative to *Adar*$^{+/-}$ mice, with the majority of upregulated genes
316 being known ISGs (136 out of 151 and 124 out of 137, respectively) (**Fig. 5B,C, Fig. S3**). These
317 outcomes suggest that *RdRp*$^{tg/-}$ *Adar*$^{+/-}$ mice have an extreme ISG response that likely leads to
318 the Singleton-Merten interferonopathy-resembling phenotype. Interestingly, when we examined
319 which genes are changing across genotype comparisons, we saw a largely overlapping set of
320 ISGs upregulated in the presence of the RdRp transgene or in the absence of one *Adar* allele
321 (**Fig. 5D**). All three non-WT genotypes (*Adar*$^{+/-}$, *RdRp*$^{tg/-}$, and *RdRp*$^{tg/-}$ *Adar*$^{+/-}$) showed significant
322 upregulation of overlapping ISGs, but the magnitude of upregulation varies drastically by
323 genotype (**Fig. 5D**). Consistently the dual heterozygotes have extremely high induction,
324 elevated 3-5-fold over what we observed in *RdRp*$^{tg/-}$ mice, although largely concordant in which

325 genes are induced, while *Adar*$^{+/-}$ have only low level ISG induction (**Fig. 5B,D**). Thus, synergy
326 between the RdRp transgene and the absence of one *Adar* allele leads to a hyper-induced ISG
327 state in mice that is no longer tolerated. We considered whether differing expression of the
328 TMEV RdRp transcript itself might be influencing the observed double heterozygote differences
329 (even though the ubiquitin C promoter controls its transcription), but the RdRp mRNA was
330 similarly elevated in both (**Fig. 5E).**
331
332 **Pathway Analysis.** Ingenuity Pathway Analysis (IPA) was used to assess which canonical
333 molecular pathways are activated or inhibited. *Adar*$^{+/-}$*, RdRp*$^{tg/-}$*,* and *RdRp*$^{tg/-}$ *Adar*$^{+/-}$ mice
334 showed activation of genes related to interferon signaling, neuroinflammatory signaling and
335 PRRs (**Fig. 5F**). Genes associated with dendritic cell (DC) maturation were activated in *RdRp*$^{tg/-}$
336 and *RdRp*$^{tg/-}$ *Adar*$^{+/-}$ mice (**Fig. 5F**). Increased DC maturation, specifically in *RdRp*$^{tg/-}$ *Adar*$^{+/-}$
337 animals, may contribute to the observed disease. We also carried out analyses of upstream
338 regulators that may be responsible for gene expression patterns. In WT-*Adar*$^{+/-}$, *RdRp*$^{tg/-}$ *Adar*$^{+/+}$*,*
339 and *RdRp*$^{tg/-}$ *Adar*$^{+/-}$ mice, we not surprisingly identified *Ddx58* (RIG-I), and *Ifih1* (MDA5) as
340 upstream regulators activated in those samples (**Fig. S4**). Main intermediates in interferon
341 signaling pathways, including IRF7, IRF9, STAT1, and STAT2 were also statistically significant
342 predicted key regulators. (**Fig. S4**). Only in mice missing one *Adar* allele (*Adar*$^{+/-}$ and *RdRp*$^{tg/-}$
343 *Adar*$^{+/-}$ mice) did we also identify predicted regulation by additional PRR proteins, including
344 TLR3, which recognizes dsRNA, and *ZBP1* (DAI), which recognizes Z-form nucleic acids (63),
345 both resulting in activation of interferon signaling (**Fig. S4**). Interactions with other nucleic acid
346 sensing molecules besides MDA5 may thus play roles in sensing of ADAR1-edited transcripts.
347
348 **Molecular and cellular differences in *RdRp*$^{tg/-}$ *Adar*$^{+/-}$ mice validate RNA-seq analyses and**
349 **are consistent with interferonopathy**. To characterize the RNA-seq results further, we
350 determined levels of ISG mRNAs in brain tissues of *Adar*$^{+/+}$ and *Adar*$^{+/-}$ mice, with or without the
351 RdRp transgene. Similar to the RNA-seq data, in *Adar*$^{+/-}$ mice, there were only small increases
352 in levels of three classical ISG mRNAs compared to WT mice (about 2- to 5-fold; **Fig. 6A**). In
353 contrast, and consistent with prior data (37-39). *RdRp*$^{tg/-}$ mice had major increases compared to
354 WT mice. However, the dual heterozygotes (*RdRp*$^{tg/-}$ *Adar*$^{+/-}$) had much higher ISG mRNA
355 elevations, on the order of 200 – 600 fold relative to WT.
356
357 Importantly too, breeding to *Ifih1*$^{-/-}$ mice demonstrated that loss of MDA5 resulted in rescue of
358 animal growth and a complete abolishment of ISG upregulation observed in *RdRp*$^{tg/-}$ *Adar*$^{+/-}$

359 animals (**Fig. S5**), reinforcing the MDA5-dependence of the phenotypes. Given the massively
360 amplified ISG transcriptional pattern in the double heterozygotes, and the immune cell activation
361 and maturation pathways enrichment observed (**Fig. 5, Fig. S6**), we next harvested the spleens
362 of 4-5 week old mice for flow cytometry analyses.
363
364 Aberrantly activated immune cell subsets are canonical autoimmune disease features and
365 identifying them would support the conclusion of a dysregulated immune state in *RdRp*$^{tg/-}$ *Adar*$^{+/-}$
366 mice. In major immune cell populations in the spleens, including B cells, T cells, neutrophils,
367 DCs, and granulocytes, we found no major differences in cell population proportions across
368 different genotypes (**Fig. S7A**). The antiviral protein BST-2 (Tetherin) is a classical ISG with a
369 high dynamic range of expression in response to type I interferon stimulation in multiple
370 mammals, including mice (64-66), and the mRNA was consistently upregulated across
371 comparisons in the RNA-seq experiments. We therefore determined cell surface BST-2 protein
372 expression in the various immune cell populations, and found it to be elevated on all cell types
373 of *RdRp*$^{tg/-}$ *Adar*$^{+/-}$ mice and was slightly upregulated on DCs in WT-*Adar*$^{+/-}$ and *RdRp*$^{tg/-}$ animals
374 and granulocytes from *RdRp*$^{tg/-}$ animals (**Fig. 6B**), similar to what we have observed previously
375 (38). We also examined monocyte and dendritic cell differentiation, maturation and activation in
376 these animals (**Fig. 6C, D, E).** Monocytes were significantly increased in *RdRp*$^{t/-}$ *Adar*$^{+/-}$ animals
377 (**Fig. 6C**) and cDC1s were slightly decreased also (**Fig. S7B**). Monocytes are circulating
378 precursor cells that infiltrate into the tissue upon detection of proinflammatory stimuli and
379 differentiate into effector monocyte-derived DCs (moDCs). An increase in this cell population is
380 suggestive of increased demand for precursor cells in these animals. In support of this
381 hypothesis, we observed increased BST-2 expression on all DC subsets from *RdRp*$^{tg/-}$ *Adar*$^{+/-}$
382 mice, as well as increased expression of the activation markers CD80/86 on *RdRp*$^{tg/-}$ *Adar*$^{+/-}$
383 monocytes and moDCs (**Fig. 6D, E**). Disorders in DC function and activity have been widely
384 implicated in several autoimmune diseases, including SLE, and may contribute to disease
385 development in *Adar*$^{+/-}$ RdRp$^{tg/-}$ animals.
386
387 The immune cell profiling above and the upregulated ISG profiles raised the question of whether
388 proinflammatory cytokines are elevated in the double heterozygotes. Indeed, transcripts for
389 IFNβ, which were undetectable at baseline in WT and Adar+/- mice, were detectably elevated,
390 but at low levels, in both RdRp$^{tg/-}$ and more so in *RdRp*$^{tg/-}$ *Adar*$^{+/-}$ mice (**Fig. S8**). While classical
391 proinflammatory cytokines such as IL6 and TNFα were not elevated in any group, several

392 proinflammatory C-C and C-X-C chemokines were, most prominently CXCL10, CXCL11, CCL2
393 and CCL5 (**Fig. S8**).
394
395 **Editome analyses show dual heterozygotes have dysregulated A-I editing**. To interrogate
396 the relationship of the loss of one *Adar* allele to the SMS-like phenotype of *RdRp*$^{tg/-}$ *Adar*$^{+/-}$ mice,
397 we characterized genome-wide A-to-I editing differences between all four genotypes of animals
398 (**Fig. 7**). We first carried out whole exome sequencing to eliminate any SNPs that may be
399 unique to our colony or genotypes (of which very few were detected), as compared to the
400 reference genome. We then identified all A-to-G changes in RNA-seq data (inosine is decoded
401 as guanine during sequencing). We found that the majority of edited sites in all four genotypes
402 were in intergenic regions and 3'UTRs, with a fractionally larger portion for 3'UTRs in RdRp^{tg}
403 mice. Exons and introns were represented approximately equivalently (**Fig. 7A, B**). Interestingly
404 and unexpectedly, while edited site locations were similarly proportioned among the four
405 genotypes (**Fig. 7A**), the number of edited sites increased substantially (50 – 65%) in *RdRp*$^{tg/-}$
406 *Adar*$^{+/-}$ mice compared to the other three genotypes (**Fig. 7B**). Numbers of edited genes also
407 increased. This seemingly paradoxical result in the Singleton-Merten-affected dual
408 heterozygotes was apparent across all gene regions. In contrast, in the *Adar*$^{+/-}$ and *RdRp*$^{tg/-}$
409 mice, the number of edited genes decreased compared to WT mice and the overall number of
410 edited sites remained largely unchanged (**Fig. 7B**). Despite the number of edited sites being
411 unchanged for WT, *Adar*$^{+/-}$, and *RdRp*$^{tg/-}$ mice, there was a shift from intergenic to extragenic
412 regions in these animals, and there was a substantial proportionate rise in 3'UTR editing in
413 RdRp$^{tg/-}$ mice of both genotypes, which was quantitatively greater in *RdRp*$^{tg/-}$ *Adar*$^{+/-}$ mice.
414
415 Because they possess only one functional *Adar* allele, it was unexpected that *RdRp*$^{tg/-}$ *Adar*$^{+/-}$
416 mice would have these increases in the number of A-to-I edited genes and A-to-I edited sites
417 (**Fig. 7B**). Thus, there is a dysregulation of A-to-I editing. When we examined overlap of edited
418 sites or edited genes between genotypes (visualized in Venn diagrams, **Fig. 7C**), we observed
419 the highest number of uniquely edited genes (719) and sites (695) in *RdRp*$^{tg/-}$ *Adar*$^{+/-}$ mice,
420 indicating that these animals have significantly different editing patterns compared to the other
421 genotypes. It is notable that *RdRp*$^{tg/-}$ *Adar*$^{+/-}$ mice have increased editing in LINEs, SINEs, DNA
422 transposons and other retrotransposons, since increases in retroelement transcription are
423 associated with autoimmune disease states (67). In addition, previous studies have shown
424 ADAR1 to be critical for regulation of retroelement transcript self-reactivity(9, 10). Increased
425 ADAR-specific editing of retroelements is normally protective, but in our double heterozygote

426 mice this alone is not compensatory enough to prevent disease, indicating that the A-to-I editing
427 process in these animals is abnormal.
428
429 Next, we used RNA-seq to analyze the changes in edited genes, along with relative expression
430 in each group of mice, to determine associations with activated/inhibited canonical pathways
431 and enriched diseases and biological functions (**Fig. S9**). Of edited mRNAs in *RdRp*$^{tg/-}$ *Adar*$^{+/-}$
432 mice, genes associated with disease and biological functions related to apoptosis, cell death,
433 and necrosis were enriched (**Fig. S9**). Notably, there was a clear reduction in genes involved in
434 inflammatory disease states that was unique to comparisons with this *RdRp*$^{tg/-}$ *Adar*$^{+/-}$ mice (**Fig.**
435 **S9**).
436
437 To explore the question further, we asked how A-to-I editing of ISG mRNAs, when it occurs,
438 affects expression of their encoded proteins in *RdRp*$^{tg/-}$ *ADAR*$^{+/-}$ mice. We measured mRNA
439 levels and performed protein immunoblotting for several ISGs that are uniquely edited in
440 *RdRp*$^{tg/-}$ *Adar*$^{+/-}$ mice: Rig-I, Isg15, and Zbp1. Both Rig-I (*Ddx58*) and Zbp1 (*Zbp1*) were also
441 predicted by the RNA-seq analysis to be key upstream gene regulators (genes with known
442 activation/inhibition effects on the enriched pathways; **Fig. S4**). Expression levels of Rig-I,
443 Isg15, and to a much lesser extent and not at the protein level, Zbp1, were increased in *RdRp*$^{tg/-}$
444 and *RdRp*$^{tg/-}$ *Adar*$^{+/-}$ mice, but not in *Adar*$^{+/-}$ mice (**Fig. 7D**,**E)** indicating that A-to-I editing does
445 not reduce expression of these ISGs. Additionally, ADAR1 isoforms were expressed in *RdRp*$^{tg/-}$
446 *Adar*$^{+/-}$ mice at relatively similar levels as their *wild type* counterpart (**Fig. 7E,F**), with slightly
447 higher p150 protein in *RdRp*$^{tg/-}$ mice and *RdRp*$^{tg/-}$*Adar*$^{+/-}$ mice. Notably, in *Adar*$^{+/-}$ mice alone, we
448 observed decreased ADAR1 protein expression (**Fig. 7F**), as would be predicted from loss of an
449 allele.

450 Endogenous retroelements are enriched in the 3' UTRs of ISG mRNAs (68). Despite the
451 increased ISG mRNA expression in *RdRp*$^{tg/-}$ *Adar*$^{+/-}$ animals compared to WT animals (**Fig. 5C**),
452 the proportion of uniquely edited sites that were within an ISG RNA versus those of other genes
453 was not significantly elevated (**Fig. S10**). This was the case despite the double heterozygotes
454 having an increase in total edited genes and sites (**Fig. 7C**). Compared to the WT and double
455 heterozygotes, *RdRp*$^{tg/-}$ and particularly *Adar*$^{+/-}$ animals had small, though significant, reductions
456 in the proportion of uniquely edited sites falling within an ISG. These results suggest that while
457 ISGs themselves were also edited, the amount of editing within the ISG mRNAs does not
458 account for the observed dysregulation of Adar editing.

459 In summary, single *Adar* allelic loss coupled with transgenic expression of the picornavirus
460 RdRp synergize to cause an extreme ISG response which produces an interferonopathy
461 remarkably similar to Singleton-Merten syndrome. This work presents a novel model for this
462 disease, which can be further studied to unlock molecular mechanisms driving the pathology.
463 The ADAR-intact model is exceptional for its paradoxical combination of tolerated MDA5
464 hyperactivity with autoimmunity resistance.
465
466

467 **DISCUSSION**

468

469 Precise regulation of intracellular RNA duplex sensing is critical for protecting mammals against
470 the Scylla of viral disease while also evading the Charybdis of autoimmunity. Confining sensing
471 to only exogenous dsRNAs via PRRs such as MDA5 is therefore a bedrock feature of healthy
472 antiviral defense. However, since MDA5 is relatively non-discriminating in its ligand preferences
473 (mainly binding to internal segments of longer dsRNA duplexes on the order of hundreds to
474 thousands of nucleotides in length), it has become clear in the past few years that an additional
475 layer of control, ADAR1 p150 editing of host cellular RNAs, is at play. Nevertheless, the
476 biological significance of the millions of A-to-I edits that modify RNA transcripts are incompletely
477 understood.

478

479 In the same year in which he published his Nobel-awarded paper on the YF17D yellow fever
480 vaccine that is still used today (69), virologist Max Theiler reported his isolation of Theiler's virus
481 and noted its similarities to poliovirus (70). Here we identify new features of a mouse model in
482 which we express the dsRNA-synthesizing enzyme of this picornavirus outside the viral context
483 in the tissues of mice, providing a continuous dsRNA stimulus to the MDA5-MAVS pathway. In
484 its strict MDA5-MAVS dependence, the model parallels the exclusively MDA5-dependent
485 pattern for sensing of replicating picornaviruses (1, 5-8). Having previously demonstrated the
486 lack of significant autoinflammatory 'cost' to the animals, we found here that $RdRp^{tg}$ mice are
487 further able to resist an autoimmune provocation of induced SLE in the BM12 model (**Fig. 1**).
488 However, the loss of a single *Adar* allele, which by itself is not discernibly harmful in our and
489 others' hands (18), breaks the autoinflammation-protected state, resulting in a severe disease
490 with progeric features, characterized by shortened lifespan, stunted growth, premature fur
491 graying, poorly developed teeth, and skeletal abnormalities, extreme ISG elevations, and
492 dysregulated and increased A-to-I editing. In addition to the accentuation of ISG hyper-
493 expression compared to $RdRp^{tg}$ mice, which may be causative in the pathology that emerged,
494 the double heterozygotes hyper-expressed mRNAs for several CC and CXC cytokines (**Fig.
495 S8**), a result that will be interesting to explore further in future studies of these mice. In contrast,
496 type I IFNs and the classical proinflammatory cytokines IL6 and TNFα were not induced to
497 higher levels by addition of the single *Adar* allele knockout.

498

499 Among ADAR1 mouse models that produce autoinflammatory pathology, this is the only one
500 with a simple haploinsufficient genotype and a wild type remaining *Adar* allele. All others are

501 either *Adar* $^{-/-}$ (which is embryonic lethal without an *Mda5* KO rescue) or utilize protein mutants
502 such as *Adar*^{P95A} or *Adar*^{E861A} [see ref. (71) for a comprehensive tabulation of existing mouse
503 models]. Relatedly, we further emphasize that the present model is nucleic acid-driven rather
504 than MDA5 GOF mutation-triggered. As such it is a mouse model in which 'endogenously'
505 synthesized RNAs generate an autoinflammatory disease via wild type MDA5, with the source
506 of the dsRNA being a genomically-integrated viral polymerase. Since loss of one *Adar* allele is
507 enough to tilt the immune system in RdRp^{tg} mice to a highly pathogenic autoinflammatory
508 outcome, it can be speculated that in some natural circumstances viral infections and the
509 inflammatory signaling cascades they induce have roles in triggering human autoinflammatory
510 diseases, particularly if they also disturb the finely regulated, complex equilibrium of A-to-I
511 editing. The RdRp$^{tg/-}$ *Adar*$^{+/-}$ model complements ADAR1 mutant mouse AGS models, which
512 differ in utilizing mutant ADAR1 proteins (72-74), and which do not incorporate a viral
513 polymerase. The pathological outcome in *RdRp*$^{tg/-}$ *Adar*$^{+/-}$ mice is variably penetrant, with about
514 half of mice severely affected, a feature that is common in human SMS kindreds (55, 62) as well
515 ADAR1 mutant protein mouse models of AGS (24, 73).
516
517 In some respects, the pathologies observed in *RdRp*$^{tg/-}$ *Adar*$^{+/-}$ mice resemble the human
518 interferonopathy SMS, with notable exceptions, e.g., the lack of aortic and valvular calcification
519 typically seen in the human syndrome (54, 55). In previous studies phenotypes resembling
520 AGS/SMS were produced by engineering mice to express the MDA5 constitutive activation
521 (GOF) mutants mG821S (75) or huR822Q (76). In mG821S mice, SMS-like features were
522 observed (75) but the model differs in that while it recapitulates skeletal defects, also seen in
523 *RdRp*$^{tg/-}$ *Adar*$^{+/-}$ mice and human SMS cases (56, 57, 59), it did not have the dental deformities
524 or the fur pigmentation abnormality we observed, nor did we see the deteriorating kidney
525 function found in mG821S mice. In the picornavirus RdRp^{tg} model, constitutive activation of WT
526 MDA5 expressed from the endogenous locus by upstream provision of sustained dsRNA
527 production is insufficient and addition of *Adar* haploinsufficiency is needed. It may thus have
528 value as a model of nucleic acid-induced autoimmunity that reflects the overwhelming majority
529 of patients, who have normal RLR proteins. In this regard, the G821S and R822W GOF MDA5
530 mutant proteins do not bind dsRNA and are always "on". This may be central to the difference.
531 Subsequent investigation of the pathology observed in *RdR*^{tg} *Adar* haploinsufficient mice will
532 ideally test a potential role for ZBP1, which has been identified as a main downstream effector
533 of autoinflammation in the context of mutant ADAR1 proteins. ADAR1 acts as an upstream

534 negative regulator of its activation, which can trigger inflammatory signaling and several
535 varieties of regulated cell death (63, 68, 77-80)
536
537 Why ADAR1, which mediates the most abundant form of RNA editing in metazoan organisms
538 (81), does not edit RdRp-synthesized RNAs sufficiently to prevent activation of WT MDA5 in the
539 $RdRp^{tg}$ but $Adar^{+/+}$ mouse is unclear and is an intriguing aspect to investigate in the future. The
540 data indicate that mammals have a means to prevent viral RdRp-synthesized dsRNA from being
541 protected (from sensing) by A-to-I editing, even when the RdRp is expressed completely outside
542 the context of actual viral replication, i.e., without the elaborate replication factory biogenesis
543 central to the life cycles of all positive strand RNA viruses (and also without Vpg protein capping
544 in the case of picornaviruses). How this occurs is a key topic for investigation in the field.
545
546 In prior reports of *Ifih1* gene duplication or mice carrying MDA5 GOF mutants, which also have
547 increased expression of ISGs and relative protection against viral diseases, the mice have been
548 shown to be more prone to either spontaneous or triggered autoimmunity (36, 42, 43, 75, 76).
549 Thus, $RdRp^{tg}$ mice may have distinctive tolerance mechanisms as evidenced by their resistance
550 to induced SLE. A component of these tolerance mechanisms may be the increase in overall
551 and effector regulatory T cells (**Fig. 1**), which are key autoimmune suppressor cells (49).
552
553 We conclude from our data that correctly regulated ADAR1 editing is a key suppressor of
554 interferonopathic outcomes in these animals. The results also suggest that modulation of
555 ADAR1 activity might potentially be of benefit in some human autoinflammatory diseases.
556 Despite loss of one allele, ADAR1 levels, specifically the levels of ADAR p150 protein were
557 increased equivalently in both $RdRp^{tg/-}$ and $RdRp^{tg/-}$ *Adar+/-* animals, indicating that disease is
558 not driven by a gene dosage effect in which low ADAR1 levels cause hypo-editing of dsRNA.
559 Consistent with this result, a dysregulation picture emerged in which the overall number of
560 edited sites and edited genes are increased in the double heterozygotes as compared to all
561 other genotypes and are abnormally distributed (**Fig. 7**). The dysregulation could contribute to
562 the severe phenotype observed, but again, the comparison of the degree of p150 elevation with
563 that of $RdRp^{tg/-}$ mice compels an interpretation that the level of induced ADAR1 protein is not
564 the main driver. For example, abnormally high levels of RNA editing have been reported in SLE
565 patients (82). When we measured the levels of proteins encoded by several uniquely edited ISG
566 transcripts in $RdRp^{tg/-}Adar^{+/-}$ mice, we did not identify an effect of the additional edits. We
567 considered whether increased ISG expression might lead to increased endogenous

568 retroelement dsRNA expression, a possibility suggested by the observed increase in editing of
569 SINES and LINES; in this regard, Zhang et al. showed that such endogenous retroelements are
570 in fact quite enriched in the 3' UTRs of ISG mRNAs (68). Here we found that multiple ISG
571 mRNAs were indeed A-to-I edited but the proportion of uniquely edited sites that were within an
572 ISG RNA versus those of other genes was not significantly elevated.
573
574 ADAR1 activity and editing changes in autoinflammatory diseases that are not directly linked to
575 ADAR1 mutations are still poorly understood, but our data indicate that simple expression of the
576 enzyme at physiological or higher levels does not equate with proper function. It will be
577 worthwhile to study changes in ADAR1 expression or dysregulation of A-to-I editing in
578 interferonopathies and other autoimmune disease not directly linked to ADAR1.
579
580 **METHODS**
581
582 **Mice and nomenclature**. RdRp transgenic mice on the C57/BL6J background have been
583 previously described (37). We here use *RdRp*$^{tg/-}$ to designate a mouse with one RdRp
584 transgene allele and one normal locus lacking the chromosome 6 transgene insertion, *RdRp*$^{tg/tg}$
585 for transgene homozygotes, and RdRp^{tg}, without italics, for the general model. *Adar*$^{+/-}$ mice on
586 the C57/BL6 background generated by Hartner et al (20). were obtained from the Jackson
587 Laboratory (MGI 3029789). There is a germline deletion of the gene region spanning exons 7-9,
588 which results in non-functional p110 and p150 proteins (20). Mice were backcrossed for two
589 generations onto our colony before use and genotypes were confirmed using protocols
590 suggested by the Jackson Laboratory. CD45.1^{+} congenic marker line mice were obtained from
591 the Jackson Laboratory (mouse strain: 002014) and crossed onto the BM12 mouse line
592 (Jackson Laboratory, 001162). Presence of the CD45.1 gene was confirmed via TransnetYX
593 genotyping service (Ptprc-2 Mut probe) and confirmed with flow cytometric staining of
594 splenocytes. BM12 genotyping was confirmed as described (45) in *Ifih1* knockout mice on a
595 B6.J background were obtained from Jackson labs (strain 015812). As much as possible,
596 littermate controls were used for direct comparison between groups. All experiments use a mix
597 of male and female mice for analysis. All experiments were performed in accordance with the
598 IACUC guidelines and approved procedures for the University of Colorado, Anschutz Medical
599 Center (IACUC protocol no. 00116). BM12 initiation of lupus like disease was done as described
600 (45). Briefly, 1x10^{8} splenocytes isolated from CD45.1^{+} BM12 in mice were injected
601 intraperitoneally into WT(CD45.2) or *RdRp*$^{tg/tg}$ (CD45.2) mice. Single cell solution in PBS or PSB

602 alone (sham) was used for injection in 250 μL total volume. Mice were euthanized at 14 days
603 post injection for disease evaluation.
604 **Animal Imaging, μCT analysis, Intraocular pressure determinations**. Femurs were
605 evaluated for length, cortical bone structure and trabecular microarchitecture using a Zeiss
606 Xradia Versa X-ray microscope-520 (μCT, Zeiss, Dublin, CA, USA; 80 kVp, 4x objective,
607 isotropic voxel size of 4 μm). Regions of interest were located at the femur mid-diaphysis (1 mm
608 tall) and the distal femur metaphysis (starting at 600 μm proximal to the epiphyseal line and
609 extending 1,000 μm proximally). Trabecular and cortical bone were segmented and analyzed
610 using Dragonfly Pro and Bone Analysis software (Object Research Systems, Montreal, Canada)
611 according to established guidelines (83). Trabecular bone parameters included bone volume
612 fraction (Tb.BV/TV), trabecular number (Tb.N), trabecular thickness (Tb.Th), and trabecular
613 separation (Tb.Sp). Cortical bone measures included cortical bone volume fraction (Ct.BV/TV),
614 total bone mineral density (TMD), and cortical porosity (Ct.Po). The bending moments of inertia
615 (Imax and Imin) which contribute to structural stiffness under bending were calculated. Hydrated
616 femurs were evaluated using three-point bending to failure as described (84, 85) to determine
617 mechanical properties (e.g., stiffness and maximum load) using a MTS Insight II benchtop tester
618 (MTS Corp., Minneapolis, MN; 250 N load cell, 5 mm/min deflection rate, 7 mm span width) and
619 analyzed using custom MATLAB code, Mathworks, Natick, MA, USA). Material properties (e.g.,
620 modulus, ultimate stress) were calculated using standard equations derived from engineering
621 beam theory (84). Intraocular pressures were measured with a handheld ocular
622 pneumotonometer (Model 30 Classic, Medtronic) as described (86).
623
624 **See Supplemental Methods for:**
625 a. Cell culture and siRNA delivery.
626 b. Bioinformatics and Computational Methods.
627 c. Flow Cytometry
628 d. Quantitative PCR and Immunoblotting
629 e. ELISAs.
630 f. Calcium Quantification
631 g. Histopathology methods and scoring
632

ACKNOWLEDGMENTS

Funding was provided by National Institutes of Health Avant-Garde grant DP1DA043915 (E.M.P.), a John H. Tietze Foundation grant (E.M.P.), and an NSF grant 1707065 (V.L.F.). We thank C. Radomile and J. Chen for technical assistance with animal experiments, the University of Colorado Denver School of Medicine (UCDSOM) Division of Allergy and Clinical Immunology Flow Cytometry Core for use of the LSRII instrument, the UCDSOM Research Histology Core Laboratory for tissue processing (RRID: SCR_021994), and the CU at Boulder Materials Instrumentation and Multimodal Imaging Core Facility (RRID: SCR_019307) for X-ray microscopy and micro-computed tomography imaging.

645 **Figure Legends**

646

647 **Figure 1. RdRp^{tg} mice resist SLE-like disease induction in the BM12 model of lupus.** Ten-
648 week-old mice were challenged with 100 million BM12-derived splenocytes. Mice were
649 harvested 14 days post challenge for analyses. **(A)** Splenomegaly. Weights of BM12 and sham-
650 injected mice spleens were measured. **(B,C)** Germinal center B cells, plasma cells and Tfh
651 cells. RBC-lysed, single cell suspensions of splenocytes from BM12 or sham injected animals
652 were generated for flow staining and germinal center B cells and plasma B cells (B), or follicular
653 helper cell populations (C) were measured by flow cytometry according to gating described in
654 materials and methods section. **(D)** Anti-nuclear antibodies. Sera from BM12 splenocyte-
655 injected or sham injected mice were used to measure anti-dsDNA antibodies and anti-SmAg
656 antibodies by quantitative ELISA. Data in A-D are from n = 7, 6, 8, 8 mice for WT (PBS),
657 *RdRp$^{tg/-}$* (PBS), WT (BM12), and *RdRp$^{tg/-}$* (BM12) groups respectively. **(E)** T_{reg} cells. RBC-lysed
658 single cell suspensions were generated from spleens of untreated, ten-week-old WT or RdRp^{tg}
659 mice (n = 5 for each group) and T_{reg} subsets were determined by flow cytometry. Data were
660 analyzed using one-way ANOVA followed by Tukey tests for (A-D) and an unpaired student's T
661 test for (E). * = $p < 0.05$, ** = $p < 0.01$, *** = $p < 0.001$, **** = $p < 0.0001$. Data points represent
662 individual animals, graphs show means with standard deviations (s.d.).

663

664 **Figure 2. ADAR p150 and ADAR p110 levels in RdRp^{tg} mice, and effects of *ADAR***
665 **knockdown on RdRp-dependent ISG expression.** RNA isolated from brains of 4 to 5 week
666 old WT or *RdRp$^{tg/-}$* mice (n = 5 for WT, 6 for *RdRp$^{tg/-}$*) was used to measure **(A)** ADAR p110 and
667 **(B)** ADAR p150 transcripts by qPCR. Data points represent individual animals, graphs shown
668 means, s.d. **(C)** Immunoblotting for ADAR p110 and ADAR p150 in 4 to 5 week old mouse WT
669 and *RdRp$^{tg/-}$* brain. n = 3 animals per genotype. **(D)** A549 cells with inducible Theiler's virus
670 RdRp (Tet-on system). Data are shown from two representative knockdowns. **(E)** RNAs isolated
671 from the parallel knockdowns done in panel D were used for qPCR analysis to determine
672 relative levels of the ISGs *OAS* and *ISG15* mRNAs. mRNAs were harvested 54 hours after
673 *ADAR*-targeting siRNA addition and 48 hours after dox addition. Comparisons were made
674 between dox-treated and dox-untreated cells and expressed as fold mRNA changes induced by
675 dox. Transfection controls (cells receiving transfection reagents but no siRNA) showed similar
676 levels of ISG induction after dox treatment as control siRNA-transfected cells, indicating lack of
677 contribution of transfected siRNAs to immune activation. Data are means and s.d. of triplicate

biological replicates with three technical replicates each. NS: not significant; * = $p < 0.05$, ** = $p < 0.01$, **** = $p < 0.0001$; unpaired Student's T test.

Figure 3. Phenotypic and histological differences in RdRp$^{tg/-}$ Adar$^{+/-}$ mice. (A) Size and coat color differences in 5-week-old, littermate *RdRp$^{tg/-}$* and *RdRp$^{tg/-}$ Adar$^{+/-}$* mice. **(B)** Weight differences between 4 week and 5-week-old littermate *RdRp$^{tg/-}$* and *RdRp$^{tg/-}$ Adar$^{+/-}$* mice (n = 9 and 5 respectively). **(C)** Dental developmental differences between *RdRp$^{tg/-}$* and *RdRp$^{tg/-}$ Adar$^{+/-}$* mice. **(D)** Survival of animals from each group, followed for 20 weeks and shown as Kaplan-Meier plot. **(E)** H & E-stained tissue sections from kidney, brain, lung, liver, heart and spleens from *RdRp$^{tg/-}$* and *RdRp$^{tg/-}$ Adar$^{+/-}$* littermate mice. Pathological grading revealed no significant scoring in *RdRp$^{tg/-}$Adar$^{+/-}$* animals. **(F)** Blood Urea nitrogen from serum from 4-5 week old animals in WT, *Adar$^{+/-}$*, *RdRp$^{tg/-}$*, *Adar$^{+/-}$RdRp$^{tg/-}$* mice. n = 5, 6, 5, 8 for WT, *Adar$^{+/-}$*, *RdRp$^{tg/-}$*, *Adar$^{+/-}$ RdRp$^{tg/-}$*, respectively. **(G)** Anti-SmAG antibodies from serum from 4-5 week old animals as measured by quantitative ELISA. Four outlier high values were seen, but two were in the WT group. n = 15, 7, 10, 9 for WT, *Adar$^{+/-}$*, *RdRp$^{tg/-}$*, *Adar$^{+/-}$ RdRp$^{tg/-}$*, respectively. Anti-dsDNA antibody levels from matched serum was below the limit of detection for all animals tested. Where not indicated, all data and tissue sections come from a mix of male and female mice. Data in (B) were analyzed by two-way ANOVA where ****$p < 0.0001$. Data in D were analyzed using a log-rank test (Mantel-Cox) where **** = $p < 0.0001$. Data in (F) and (G) were analyzed by one-way ANOVA where *$p < 0.05$; data points represent individual animals, graphs show means and s.d.

Figure 4. Skeletal and dental features of wild type, *RdRp$^{tg/-}$*, *Adar$^{+/-}$*, and *Adar$^{+/-}$ RdRp$^{tg/-}$* mice. Femurs from 6-week-old animals were manually de-fleshed and used for all analyses. **(A)** Femur lengths of WT, *Adar$^{+/-}$*, *RdRp$^{tg/-}$*, and *RdRp$^{tg/-}$ Adar$^{+/-}$* mice (n = 8, 6, 10, and 17 animals respectively). **(B)** Representative µCT images, distal femur sections and whole bone. **(C)** Cortical bone volume fraction (BV/TV), n = 8, 7, 10, 17. **(D)** Trabecular number, n = 8, 7, 9, 17. **(E)** Trabecular separation, n = 8, 7, 9, 17. **(F)** Stiffness, n = 8, 7, 10, 15. **(G)** Maximum load, n = 8, 7, 10, 17. **(H)** Cortical total mineral density, n = 8, 7, 10, 17. **(I)** Modulus, n = 8, 7, 10, 17. **(J)** Ultimate stress, n = 8, 7, 10, 17. Mice with gray fur are indicated by light-blue symbols. Data were analyzed first by using a ROUT test to remove outliers (Q = 1%), which resulted in removal of two mice from one group in one panel (the *RdRp$^{tg/-}$ Adar$^{+/-}$* group in Fig. 4F, stiffness testing; hence there are 15 mice as opposed to the 17 for this genotype in the other panels). A one-way ANOVA comparing *RdRp$^{tg/-}$ Adar$^{+/-}$* to each other group was used followed by a Tukey tests

712 where * = $p < 0.05$, ** = $p < 0.01$, *** = $p < 0.001$, **** = $p < 0.0001$. Data points represent
713 individual animals, horizontal bars indicate means.
714
715 **Figure 5. RNA-seq analysis reveals clear pattern of ISG upregulation suggestive of an**
716 **interferonopathy.** RNA-seq from neuronal tissue from n = 4 age-matched (5 weeks) mice per
717 group. Where possible, littermate controls were used for analysis. Two male and two female
718 mice were used per group. **(A)** Multi-dimensional scaling plot of RNA expression profiles in WT-
719 WT, *Adar*$^{+/-}$, *RdRp*$^{tg/-}$, and *RdRp*$^{tg/-}$ *Adar*$^{+/-}$ mice. **(B)** Heatmap of differentially expressed ISGs
720 across the four genotypes (**Fig. S3** shows an enlarged version with gene names annotated).
721 FPKM values were log transformed with 1 pseudocount to facilitate visualization. **(C)** Summary
722 table of differentially expressed genes (DEGs) and proportions of which are known ISGs as
723 determined by the Interferome database. **(D)** Differentially expressed genes that are shared
724 across all group comparisons. **(E)** RdRp mRNA abundance in the four genotypes. **(F)**
725 Canonical molecular pathways from IPA that are significant across group comparisons.
726
727 **Figure 6. ISG and leukocyte subset differences in RdRp$^{tg/-}$ Adar$^{+/-}$ mice. (A)** qPCR of three
728 representative ISGs (*Ifit1*, *Isg15*, and *Oasl2*) in brain tissue of 4-5 week old WT, *Adar*$^{+/-}$, *RdRp*$^{tg/}$,
729 and *RdRp*$^{tg/-}$ *Adar*$^{+/-}$ mice (n = 5, 5, 6, 5, respectively). **(B-E)** Flow cytometry analysis of cellular
730 populations derived from the spleens of 4-5 week old mice. Single cell, RBC-lysed solutions
731 were prepared for use in analysis. **(B)** BST-2 expression on the main immune cell subsets in the
732 spleen including T cells (CD3$^+$), B cells (CD19$^+$), DCs (CD11c$^+$), granulocytes (Ly6G$^+$), and NK
733 cells (NKp46$^+$). n = 7, 7, 4, 4 for WT, *Adar*$^{+/-}$, *RdRp*$^{tg/}$, *RdRp*$^{tg/-}$ *Adar*$^{+/-}$, respectively. **(C)**
734 Monocytes populations across all four groups. **(D)** BST-2 expression on monocyte/DC cell
735 subsets including monocytes, cDC1s, cDC2s, and moDCs. **(D)** Activation (CD80/86 expression)
736 of monocyte/DC subsets including monocytes, cDC1s, cDC2s, and moDCs. C-E: n = 12, 7, 10,
737 8 for WT, *Adar*$^{+/-}$, *RdRp*$^{tg/}$, *RdRp*$^{tg/-}$ *Adar*$^{+/-}$, respectively. For all graphs shown, data were
738 analyzed using a one-way ANOVA followed by a Tukey tests to determine significance where *
739 = $p < 0.05$, ** = $p < 0.01$, *** = $p < 0.001$, **** = $p < 0.0001$. Data points represent individual
740 animals with the mean and s.d. shown as bars.
741
742 **Figure 7. Analysis of the A-to-I editome reveals increased editing in *RdRp*$^{tg/-}$ *Adar*$^{+/-}$ mice.**
743 Changes in A-to-I edits were determined via comparison of RNA-seq data with whole exome
744 DNA sequencing. **(A)** Pie charts showing the proportion of editing sites within a given RNA
745 element for each mouse genotype. **(B)** Table summary of the distribution of overall numbers of

746 edited genes and sites for each genotype and the breakdown of locations of the edit sites
747 among different RNA elements. For each of the four genotypes, four animals were sequenced
748 and to be counted a gene must have been edited in all four animals sequenced but editing can
749 occur anywhere in the gene. For sites, identical sites must be edited in all four animals of a
750 genotype. **(C)** Venn diagrams showing overlap of edited genes (top) or sites (bottom) among the
751 four genotypes. **(D,E)** Immunoblot analysis from two animals per group (D) and gene expression
752 fold change (E) of three *Adar*$^{+/-}$ *RdRp*$^{tg/-}$ uniquely edited genes in the RNA-seq data set (as
753 compared to WT) in 5-week-old neuronal tissue. Rig-I, Isg15, and Zbp1 were evaluated as they
754 are each ISGs that are highly upregulated in mice expressing RdRp and are key regulators of
755 the antiviral response. **(F)** Expression of *Adar* isoforms in neuronal tissue of 4-5 week old mice
756 from all four genotypes, as determined by western blot (n = 2 per group).
757
758
759

References

1. Rehwinkel J, Gack MU. 2020. RIG-I-like receptors: their regulation and roles in RNA sensing. Nat Rev Immunol 20:537-551.
2. Hornung V, Ellegast J, Kim S, Brzozka K, Jung A, Kato H, Poeck H, Akira S, Conzelmann KK, Schlee M, Endres S, Hartmann G. 2006. 5'-Triphosphate RNA is the ligand for RIG-I. Science 314:994-7.
3. Kato H, Takeuchi O, Mikamo-Satoh E, Hirai R, Kawai T, Matsushita K, Hiiragi A, Dermody TS, Fujita T, Akira S. 2008. Length-dependent recognition of double-stranded ribonucleic acids by retinoic acid-inducible gene-I and melanoma differentiation-associated gene 5. J Exp Med 205:1601-10.
4. del Toro Duany Y, Wu B, Hur S. 2015. MDA5-filament, dynamics and disease. Curr Opin Virol 12:20-5.
5. Dias Junior AG, Sampaio NG, Rehwinkel J. 2019. A Balancing Act: MDA5 in Antiviral Immunity and Autoinflammation. Trends Microbiol 27:75-85.
6. Kato H, Takeuchi O, Sato S, Yoneyama M, Yamamoto M, Matsui K, Uematsu S, Jung A, Kawai T, Ishii KJ, Yamaguchi O, Otsu K, Tsujimura T, Koh CS, Reis e Sousa C, Matsuura Y, Fujita T, Akira S. 2006. Differential roles of MDA5 and RIG-I helicases in the recognition of RNA viruses. Nature 441:101-5.
7. Gitlin L, Barchet W, Gilfillan S, Cella M, Beutler B, Flavell RA, Diamond MS, Colonna M. 2006. Essential role of mda-5 in type I IFN responses to polyriboinosinic:polyribocytidylic acid and encephalomyocarditis picornavirus. Proc Natl Acad Sci U S A 103:8459-64.
8. Feng Q, Hato SV, Langereis MA, Zoll J, Virgen-Slane R, Peisley A, Hur S, Semler BL, van Rij RP, van Kuppeveld FJ. 2012. MDA5 detects the double-stranded RNA replicative form in picornavirus-infected cells. Cell Rep 2:1187-96.
9. Ahmad S, Mu X, Yang F, Greenwald E, Park JW, Jacob E, Zhang CZ, Hur S. 2018. Breaching Self-Tolerance to Alu Duplex RNA Underlies MDA5-Mediated Inflammation. Cell 172:797-810 e13.
10. Chung H, Calis JJA, Wu X, Sun T, Yu Y, Sarbanes SL, Dao Thi VL, Shilvock AR, Hoffmann HH, Rosenberg BR, Rice CM. 2018. Human ADAR1 Prevents Endogenous RNA from Triggering Translational Shutdown. Cell 172:811-824 e14.
11. Crow YJ, Manel N. 2015. Aicardi-Goutieres syndrome and the type I interferonopathies. Nature reviews Immunology 15:429-40.
12. Crow YJ, Stetson DB. 2021. The type I interferonopathies: 10 years on. Nat Rev Immunol doi:10.1038/s41577-021-00633-9.
13. Hartner JC, Walkley CR, Lu J, Orkin SH. 2009. ADAR1 is essential for the maintenance of hematopoiesis and suppression of interferon signaling. Nat Immunol 10:109-15.
14. Rice GI, Kasher PR, Forte GM, Mannion NM, Greenwood SM, Szynkiewicz M, Dickerson JE, Bhaskar SS, Zampini M, Briggs TA, Jenkinson EM, Bacino CA, Battini R, Bertini E, Brogan PA, Brueton LA, Carpanelli M, De Laet C, de Lonlay P, del Toro M, Desguerre I, Fazzi E, Garcia-Cazorla A, Heiberg A, Kawaguchi M, Kumar R, Lin JP, Lourenco CM, Male AM, Marques W, Jr., Mignot C, Olivieri I, Orcesi S, Prabhakar P, Rasmussen M, Robinson RA, Rozenberg F, Schmidt JL, Steindl K, Tan TY, van der Merwe WG, Vanderver A, Vassallo G, Wakeling EL, Wassmer E, Whittaker E, Livingston JH, Lebon P, Suzuki T, McLaughlin PJ, et al. 2012. Mutations in ADAR1 cause Aicardi-Goutieres syndrome associated with a type I interferon signature. Nature genetics 44:1243-8.
15. Mannion NM, Greenwood SM, Young R, Cox S, Brindle J, Read D, Nellaker C, Vesely C, Ponting CP, McLaughlin PJ, Jantsch MF, Dorin J, Adams IR, Scadden AD, Ohman M, Keegan LP, O'Connell MA. 2014. The RNA-editing enzyme ADAR1 controls innate immune responses to RNA. Cell Rep 9:1482-94.

16. Samuel CE. 2019. Adenosine deaminase acting on RNA (ADAR1), a suppressor of double-stranded RNA-triggered innate immune responses. J Biol Chem 294:1710-1720.
17. Song B, Shiromoto Y, Minakuchi M, Nishikura K. 2022. The role of RNA editing enzyme ADAR1 in human disease. Wiley Interdiscip Rev RNA 13:e1665.
18. Liddicoat BJ, Piskol R, Chalk AM, Ramaswami G, Higuchi M, Hartner JC, Li JB, Seeburg PH, Walkley CR. 2015. RNA editing by ADAR1 prevents MDA5 sensing of endogenous dsRNA as nonself. Science 349:1115-20.
19. George CX, Ramaswami G, Li JB, Samuel CE. 2016. Editing of Cellular Self-RNAs by Adenosine Deaminase ADAR1 Suppresses Innate Immune Stress Responses. J Biol Chem 291:6158-68.
20. Hartner JC, Schmittwolf C, Kispert A, Muller AM, Higuchi M, Seeburg PH. 2004. Liver disintegration in the mouse embryo caused by deficiency in the RNA-editing enzyme ADAR1. J Biol Chem 279:4894-902.
21. Higuchi M, Maas S, Single FN, Hartner J, Rozov A, Burnashev N, Feldmeyer D, Sprengel R, Seeburg PH. 2000. Point mutation in an AMPA receptor gene rescues lethality in mice deficient in the RNA-editing enzyme ADAR2. Nature 406:78-81.
22. Tan MH, Li Q, Shanmugam R, Piskol R, Kohler J, Young AN, Liu KI, Zhang R, Ramaswami G, Ariyoshi K, Gupte A, Keegan LP, George CX, Ramu A, Huang N, Pollina EA, Leeman DS, Rustighi A, Goh YPS, Consortium GT, Laboratory DA, Coordinating Center -Analysis Working G, Statistical Methods groups-Analysis Working G, Enhancing Gg, Fund NIHC, Nih/Nci, Nih/Nhgri, Nih/Nimh, Nih/Nida, Biospecimen Collection Source Site N, Biospecimen Collection Source Site R, Biospecimen Core Resource V, Brain Bank Repository-University of Miami Brain Endowment B, Leidos Biomedical-Project M, Study E, Genome Browser Data I, Visualization EBI, Genome Browser Data I, Visualization-Ucsc Genomics Institute UoCSC, Chawla A, Del Sal G, Peltz G, Brunet A, Conrad DF, Samuel CE, O'Connell MA, Walkley CR, Nishikura K, Li JB. 2017. Dynamic landscape and regulation of RNA editing in mammals. Nature 550:249-254.
23. Crowl JT, Gray EE, Pestal K, Volkman HE, Stetson DB. 2017. Intracellular Nucleic Acid Detection in Autoimmunity. Annu Rev Immunol 35:313-336.
24. Heraud-Farlow JE, Walkley CR. 2020. What do editors do? Understanding the physiological functions of A-to-I RNA editing by adenosine deaminase acting on RNAs. Open Biol 10:200085.
25. Nakahama T, Kawahara Y. 2023. The RNA-editing enzyme ADAR1: a regulatory hub that tunes multiple dsRNA-sensing pathways. Int Immunol 35:123-133.
26. Heraud-Farlow JE, Chalk AM, Linder SE, Li Q, Taylor S, White JM, Pang L, Liddicoat BJ, Gupte A, Li JB, Walkley CR. 2017. Protein recoding by ADAR1-mediated RNA editing is not essential for normal development and homeostasis. Genome Biol 18:166.
27. Chalk AM, Taylor S, Heraud-Farlow JE, Walkley CR. 2019. The majority of A-to-I RNA editing is not required for mammalian homeostasis. Genome Biol 20:268.
28. Stetson DB, Ko JS, Heidmann T, Medzhitov R. 2008. Trex1 prevents cell-intrinsic initiation of autoimmunity. Cell 134:587-98.
29. Crow YJ, Leitch A, Hayward BE, Garner A, Parmar R, Griffith E, Ali M, Semple C, Aicardi J, Babul-Hirji R, Baumann C, Baxter P, Bertini E, Chandler KE, Chitayat D, Cau D, Dery C, Fazzi E, Goizet C, King MD, Klepper J, Lacombe D, Lanzi G, Lyall H, Martinez-Frias ML, Mathieu M, McKeown C, Monier A, Oade Y, Quarrell OW, Rittey CD, Rogers RC, Sanchis A, Stephenson JB, Tacke U, Till M, Tolmie JL, Tomlin P, Voit T, Weschke B, Woods CG, Lebon P, Bonthron DT, Ponting CP, Jackson AP. 2006. Mutations in genes encoding ribonuclease H2 subunits cause Aicardi-Goutieres syndrome and mimic congenital viral brain infection. Nat Genet 38:910-6.
30. Crow YJ, Hayward BE, Parmar R, Robins P, Leitch A, Ali M, Black DN, van Bokhoven H, Brunner HG, Hamel BC, Corry PC, Cowan FM, Frints SG, Klepper J, Livingston JH,

Lynch SA, Massey RF, Meritet JF, Michaud JL, Ponsot G, Voit T, Lebon P, Bonthron DT, Jackson AP, Barnes DE, Lindahl T. 2006. Mutations in the gene encoding the 3'-5' DNA exonuclease TREX1 cause Aicardi-Goutieres syndrome at the AGS1 locus. Nat Genet 38:917-20.

31. Rice GI, Del Toro Duany Y, Jenkinson EM, Forte GM, Anderson BH, Ariaudo G, Bader-Meunier B, Baildam EM, Battini R, Beresford MW, Casarano M, Chouchane M, Cimaz R, Collins AE, Cordeiro NJ, Dale RC, Davidson JE, De Waele L, Desguerre I, Faivre L, Fazzi E, Isidor B, Lagae L, Latchman AR, Lebon P, Li C, Livingston JH, Lourenco CM, Mancardi MM, Masurel-Paulet A, McInnes IB, Menezes MP, Mignot C, O'Sullivan J, Orcesi S, Picco PP, Riva E, Robinson RA, Rodriguez D, Salvatici E, Scott C, Szybowska M, Tolmie JL, Vanderver A, Vanhulle C, Vieira JP, Webb K, Whitney RN, Williams SG, Wolfe LA, et al. 2014. Gain-of-function mutations in IFIH1 cause a spectrum of human disease phenotypes associated with upregulated type I interferon signaling. Nat Genet 46:503-509.

32. Oda H, Nakagawa K, Abe J, Awaya T, Funabiki M, Hijikata A, Nishikomori R, Funatsuka M, Ohshima Y, Sugawara Y, Yasumi T, Kato H, Shirai T, Ohara O, Fujita T, Heike T. 2014. Aicardi-Goutieres syndrome is caused by IFIH1 mutations. Am J Hum Genet 95:121-5.

33. Uggenti C, Lepelley A, Depp M, Badrock AP, Rodero MP, El-Daher MT, Rice GI, Dhir S, Wheeler AP, Dhir A, Albawardi W, Fremond ML, Seabra L, Doig J, Blair N, Martin-Niclos MJ, Della Mina E, Rubio-Roldan A, Garcia-Perez JL, Sproul D, Rehwinkel J, Hertzog J, Boland-Auge A, Olaso R, Deleuze JF, Baruteau J, Brochard K, Buckley J, Cavallera V, Cereda C, De Waele LMH, Dobbie A, Doummar D, Elmslie F, Koch-Hogrebe M, Kumar R, Lamb K, Livingston JH, Majumdar A, Lorenco CM, Orcesi S, Peudenier S, Rostasy K, Salmon CA, Scott C, Tonduti D, Touati G, Valente M, van der Linden H, Jr., Van Esch H, et al. 2020. cGAS-mediated induction of type I interferon due to inborn errors of histone pre-mRNA processing. Nat Genet 52:1364-1372.

34. Wang Q, Khillan J, Gadue P, Nishikura K. 2000. Requirement of the RNA editing deaminase ADAR1 gene for embryonic erythropoiesis. Science 290:1765-8.

35. Wang Q, Miyakoda M, Yang W, Khillan J, Stachura DL, Weiss MJ, Nishikura K. 2004. Stress-induced apoptosis associated with null mutation of ADAR1 RNA editing deaminase gene. J Biol Chem 279:4952-61.

36. Funabiki M, Kato H, Miyachi Y, Toki H, Motegi H, Inoue M, Minowa O, Yoshida A, Deguchi K, Sato H, Ito S, Shiroishi T, Takeyasu K, Noda T, Fujita T. 2014. Autoimmune Disorders Associated with Gain of Function of the Intracellular Sensor MDA5. Immunity 40:199-212.

37. Painter MM, Morrison JH, Zoecklein LJ, Rinkoski TA, Watzlawik JO, Papke LM, Warrington AE, Bieber AJ, Matchett WE, Turkowski KL, Poeschla EM, Rodriguez M. 2015. Antiviral Protection via RdRP-Mediated Stable Activation of Innate Immunity. PLoS Pathogens 11:e1005311.

38. Miller CM, Barrett BS, Chen J, Morrison JH, Radomile C, Santiago ML, Poeschla EM. 2020. Systemic Expression of a Viral RdRP Protects against Retrovirus Infection and Disease. Journal of Virology 94.

39. Bankers L, Miller C, Liu G, Thongkittidilok C, Morrison J, Poeschla EM. 2020. Development of interferon-stimulated gene expression from embryogenesis through adulthood, with and without constitutive MDA5 pathway activation. Journal of Immunology 204:2791-2807.

40. Kerkvliet J, Papke L, Rodriguez M. 2011. Antiviral effects of a transgenic RNA-dependent RNA polymerase. J Virol 85:621-5.

41. Kerkvliet J, Zoecklein L, Papke L, Denic A, Bieber AJ, Pease LR, David CS, Rodriguez M. 2009. Transgenic expression of the 3D polymerase inhibits Theiler's virus infection and demyelination. J Virol 83:12279-89.
42. Crampton SP, Deane JA, Feigenbaum L, Bolland S. 2012. Ifih1 gene dose effect reveals MDA5-mediated chronic type I IFN gene signature, viral resistance, and accelerated autoimmunity. J Immunol 188:1451-9.
43. Gorman JA, Hundhausen C, Errett JS, Stone AE, Allenspach EJ, Ge Y, Arkatkar T, Clough C, Dai X, Khim S, Pestal K, Liggitt D, Cerosaletti K, Stetson DB, James RG, Oukka M, Concannon P, Gale M, Jr., Buckner JH, Rawlings DJ. 2017. The A946T variant of the RNA sensor IFIH1 mediates an interferon program that limits viral infection but increases the risk for autoimmunity. Nat Immunol 18:744-752.
44. Morris SC, Cohen PL, Eisenberg RA. 1990. Experimental induction of systemic lupus erythematosus by recognition of foreign Ia. Clin Immunol Immunopathol 57:263-73.
45. Klarquist J, Janssen EM. 2015. The bm12 Inducible Model of Systemic Lupus Erythematosus (SLE) in C57BL/6 Mice. J Vis Exp doi:10.3791/53319:e53319.
46. Stebegg M, Kumar SD, Silva-Cayetano A, Fonseca VR, Linterman MA, Graca L. 2018. Regulation of the Germinal Center Response. Front Immunol 9:2469.
47. Tsokos GC, Lo MS, Costa Reis P, Sullivan KE. 2016. New insights into the immunopathogenesis of systemic lupus erythematosus. Nat Rev Rheumatol 12:716-730.
48. Zhuang H, Szeto C, Han S, Yang L, Reeves WH. 2015. Animal Models of Interferon Signature Positive Lupus. Front Immunol 6:291.
49. Dominguez-Villar M, Hafler DA. 2018. Regulatory T cells in autoimmune disease. Nat Immunol 19:665-673.
50. Kim J, Lahl K, Hori S, Loddenkemper C, Chaudhry A, deRoos P, Rudensky A, Sparwasser T. 2009. Cutting edge: depletion of Foxp3+ cells leads to induction of autoimmunity by specific ablation of regulatory T cells in genetically targeted mice. J Immunol 183:7631-4.
51. Sun T, Yu Y, Wu X, Acevedo A, Luo JD, Wang J, Schneider WM, Hurwitz B, Rosenberg BR, Chung H, Rice CM. 2021. Decoupling expression and editing preferences of ADAR1 p150 and p110 isoforms. Proc Natl Acad Sci U S A 118.
52. George CX, Samuel CE. 1999. Human RNA-specific adenosine deaminase ADAR1 transcripts possess alternative exon 1 structures that initiate from different promoters, one constitutively active and the other interferon inducible. Proc Natl Acad Sci U S A 96:4621-6.
53. Yang JH, Nie Y, Zhao Q, Su Y, Pypaert M, Su H, Rabinovici R. 2003. Intracellular localization of differentially regulated RNA-specific adenosine deaminase isoforms in inflammation. J Biol Chem 278:45833-42.
54. Singleton EB, Merten DF. 1973. An unusual syndrome of widened medullary cavities of the metacarpals and phalanges, aortic calcification and abnormal dentition. Pediatr Radiol 1:2-7.
55. Feigenbaum A, Muller C, Yale C, Kleinheinz J, Jezewski P, Kehl HG, MacDougall M, Rutsch F, Hennekam RC. 2013. Singleton-Merten syndrome: an autosomal dominant disorder with variable expression. Am J Med Genet A 161A:360-70.
56. Rutsch F, MacDougall M, Lu C, Buers I, Mamaeva O, Nitschke Y, Rice GI, Erlandsen H, Kehl HG, Thiele H, Nurnberg P, Hohne W, Crow YJ, Feigenbaum A, Hennekam RC. 2015. A specific IFIH1 gain-of-function mutation causes Singleton-Merten syndrome. Am J Hum Genet 96:275-82.
57. Pettersson M, Bergendal B, Norderyd J, Nilsson D, Anderlid BM, Nordgren A, Lindstrand A. 2017. Further evidence for specific IFIH1 mutation as a cause of Singleton-Merten syndrome with phenotypic heterogeneity. Am J Med Genet A 173:1396-1399.

58. Bursztejn AC, Briggs TA, del Toro Duany Y, Anderson BH, O'Sullivan J, Williams SG, Bodemer C, Fraitag S, Gebhard F, Leheup B, Lemelle I, Oojageer A, Raffo E, Schmitt E, Rice GI, Hur S, Crow YJ. 2015. Unusual cutaneous features associated with a heterozygous gain-of-function mutation in IFIH1: overlap between Aicardi-Goutieres and Singleton-Merten syndromes. Br J Dermatol 173:1505-13.
59. Buers I, Rice GI, Crow YJ, Rutsch F. 2017. MDA5-Associated Neuroinflammation and the Singleton-Merten Syndrome: Two Faces of the Same Type I Interferonopathy Spectrum. J Interferon Cytokine Res 37:214-219.
60. de Carvalho LM, Ngoumou G, Park JW, Ehmke N, Deigendesch N, Kitabayashi N, Melki I, Souza FFL, Tzschach A, Nogueira-Barbosa MH, Ferriani V, Louzada-Junior P, Marques W, Jr., Lourenco CM, Horn D, Kallinich T, Stenzel W, Hur S, Rice GI, Crow YJ. 2017. Musculoskeletal Disease in MDA5-Related Type I Interferonopathy: A Mendelian Mimic of Jaccoud's Arthropathy. Arthritis Rheumatol 69:2081-2091.
61. Xiao W, Feng J, Long H, Xiao B, Luo ZH. 2021. Case Report: Aicardi-Goutieres Syndrome and Singleton-Merten Syndrome Caused by a Gain-of-Function Mutation in IFIH1. Front Genet 12:660953.
62. Jang MA, Kim EK, Now H, Nguyen NT, Kim WJ, Yoo JY, Lee J, Jeong YM, Kim CH, Kim OH, Sohn S, Nam SH, Hong Y, Lee YS, Chang SA, Jang SY, Kim JW, Lee MS, Lim SY, Sung KS, Park KT, Kim BJ, Lee JH, Kim DK, Kee C, Ki CS. 2015. Mutations in DDX58, which encodes RIG-I, cause atypical Singleton-Merten syndrome. Am J Hum Genet 96:266-74.
63. Maelfait J, Rehwinkel J. 2023. The Z-nucleic acid sensor ZBP1 in health and disease. J Exp Med 220.
64. Neil SJ, Zang T, Bieniasz PD. 2008. Tetherin inhibits retrovirus release and is antagonized by HIV-1 Vpu. Nature 451:425-30.
65. Liberatore RA, Bieniasz PD. 2011. Tetherin is a key effector of the antiretroviral activity of type I interferon in vitro and in vivo. Proc Natl Acad Sci U S A 108:18097-101.
66. Morrison JH, Poeschla EM. 2023. The Feline Immunodeficiency Virus Envelope Signal Peptide Is a Tetherin Antagonizing Protein. mBio 14:e0016123.
67. Kassiotis G, Stoye JP. 2016. Immune responses to endogenous retroelements: taking the bad with the good. Nat Rev Immunol 16:207-19.
68. Zhang T, Yin C, Fedorov A, Qiao L, Bao H, Beknazarov N, Wang S, Gautam A, Williams RM, Crawford JC, Peri S, Studitsky V, Beg AA, Thomas PG, Walkley C, Xu Y, Poptsova M, Herbert A, Balachandran S. 2022. ADAR1 masks the cancer immunotherapeutic promise of ZBP1-driven necroptosis. Nature 606:594-602.
69. Theiler M, Smith HH. 1937. The Use of Yellow Fever Virus Modified by in Vitro Cultivation for Human Immunization. J Exp Med 65:787-800.
70. Theiler M. 1937. Spontaneous Encephalomyelitis of Mice, a New Virus Disease. J Exp Med 65:705-19.
71. Rehwinkel J, Mehdipour P. 2024. ADAR1: from basic mechanisms to inhibitors. Trends Cell Biol doi:10.1016/j.tcb.2024.06.006.
72. Maurano M, Snyder JM, Connelly C, Henao-Mejia J, Sidrauski C, Stetson DB. 2021. Protein kinase R and the integrated stress response drive immunopathology caused by mutations in the RNA deaminase ADAR1. Immunity 54:1948-1960 e5.
73. Liang Z, Chalk AM, Taylor S, Goradia A, Heraud-Farlow JE, Walkley CR. 2023. The phenotype of the most common human ADAR1p150 Zalpha mutation P193A in mice is partially penetrant. EMBO Rep doi:10.15252/embr.202255835:e55835.
74. Guo X, Steinman RA, Sheng Y, Cao G, Wiley CA, Wang Q. 2022. An AGS-associated mutation in ADAR1 catalytic domain results in early-onset and MDA5-dependent encephalopathy with IFN pathway activation in the brain. J Neuroinflammation 19:285.

1011 75. Soda N, Sakai N, Kato H, Takami M, Fujita T. 2019. Singleton-Merten Syndrome-like
1012 Skeletal Abnormalities in Mice with Constitutively Activated MDA5. J Immunol 203:1356-
1013 1368.
1014 76. Emralino FL, Satoh S, Sakai N, Takami M, Takeuchi F, Yan N, Rutsch F, Fujita T, Kato
1015 H. 2022. Double-Stranded RNA Induces Mortality in an MDA5-Mediated Type I
1016 Interferonopathy Model. J Immunol 209:2093-2103.
1017 77. Karki R, Sundaram B, Sharma BR, Lee S, Malireddi RKS, Nguyen LN, Christgen S,
1018 Zheng M, Wang Y, Samir P, Neale G, Vogel P, Kanneganti TD. 2021. ADAR1 restricts
1019 ZBP1-mediated immune response and PANoptosis to promote tumorigenesis. Cell Rep
1020 37:109858.
1021 78. Hubbard NW, Ames JM, Maurano M, Chu LH, Somfleth KY, Gokhale NS, Werner M,
1022 Snyder JM, Lichauco K, Savan R, Stetson DB, Oberst A. 2022. ADAR1 mutation causes
1023 ZBP1-dependent immunopathology. Nature 607:769-775.
1024 79. Jiao H, Wachsmuth L, Wolf S, Lohmann J, Nagata M, Kaya GG, Oikonomou N, Kondylis
1025 V, Rogg M, Diebold M, Troder SE, Zevnik B, Prinz M, Schell C, Young GR, Kassiotis G,
1026 Pasparakis M. 2022. ADAR1 averts fatal type I interferon induction by ZBP1. Nature
1027 607:776-783.
1028 80. de Reuver R, Verdonck S, Dierick E, Nemegeer J, Hessmann E, Ahmad S, Jans M,
1029 Blancke G, Van Nieuwerburgh F, Botzki A, Vereecke L, van Loo G, Declercq W, Hur S,
1030 Vandenabeele P, Maelfait J. 2022. ADAR1 prevents autoinflammation by suppressing
1031 spontaneous ZBP1 activation. Nature 607:784-789.
1032 81. Eisenberg E, Levanon EY. 2018. A-to-I RNA editing - immune protector and
1033 transcriptome diversifier. Nat Rev Genet 19:473-490.
1034 82. Roth SH, Danan-Gotthold M, Ben-Izhak M, Rechavi G, Cohen CJ, Louzoun Y, Levanon
1035 EY. 2018. Increased RNA Editing May Provide a Source for Autoantigens in Systemic
1036 Lupus Erythematosus. Cell Rep 23:50-57.
1037 83. Bouxsein ML, Boyd SK, Christiansen BA, Guldberg RE, Jepsen KJ, Muller R. 2010.
1038 Guidelines for assessment of bone microstructure in rodents using micro-computed
1039 tomography. J Bone Miner Res 25:1468-86.
1040 84. Schriefer JL, Robling AG, Warden SJ, Fournier AJ, Mason JJ, Turner CH. 2005. A
1041 comparison of mechanical properties derived from multiple skeletal sites in mice. J
1042 Biomech 38:467-75.
1043 85. Heveran CM, Schurman CA, Acevedo C, Livingston EW, Howe D, Schaible EG, Hunt
1044 HB, Rauff A, Donnelly E, Carpenter RD, Levi M, Lau AG, Bateman TA, Alliston T, King
1045 KB, Ferguson VL. 2019. Chronic kidney disease and aging differentially diminish bone
1046 material and microarchitecture in C57Bl/6 mice. Bone 127:91-103.
1047 86. Barraza RA, McLaren JW, Poeschla EM. 2010. Prostaglandin Pathway Gene Therapy
1048 for Sustained Reduction of Intraocular Pressure. Molecular Therapy 18:491-501.

1049

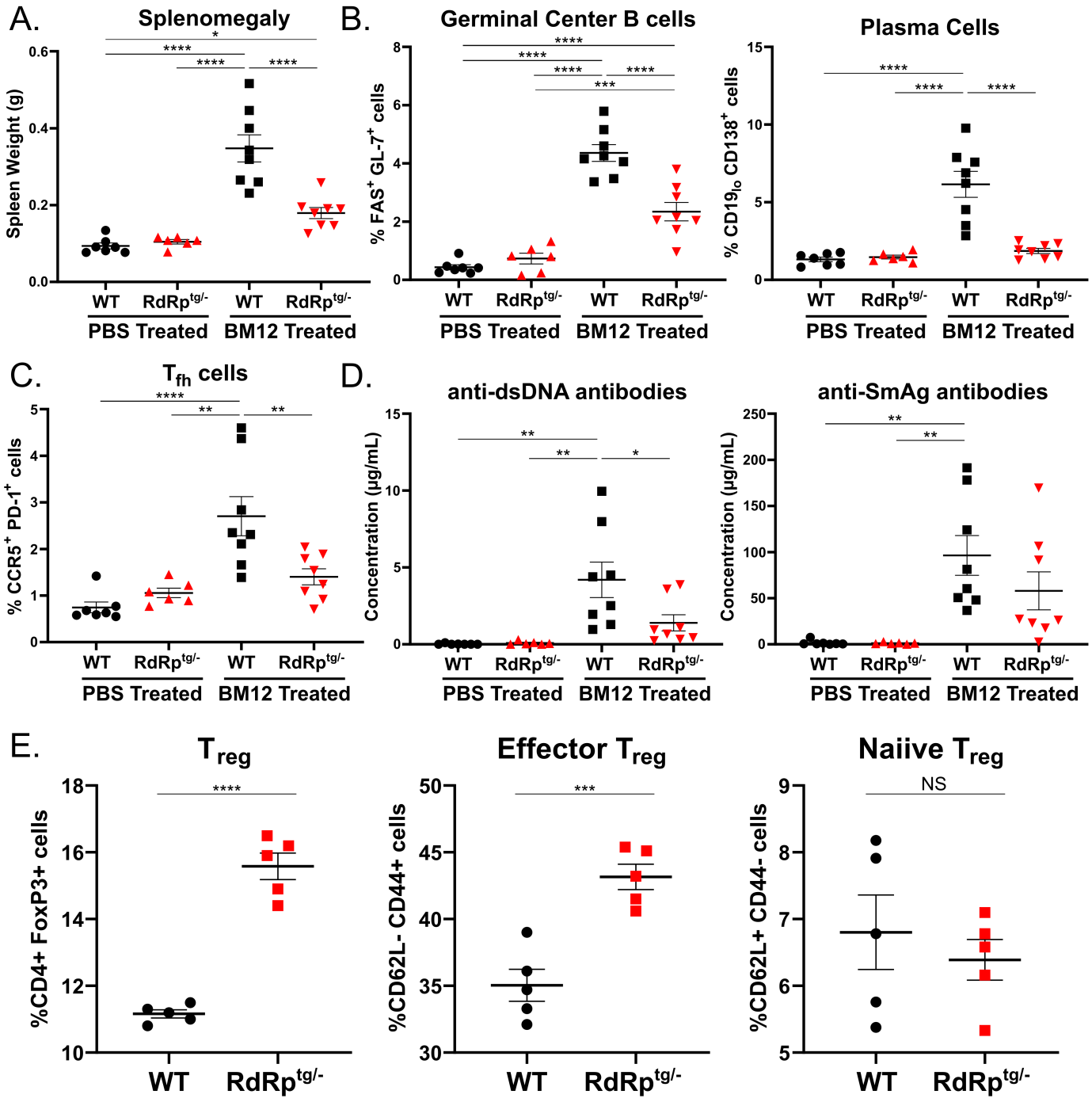
A.
Splenomegaly
Spleen Weight (g)
0.0
0.2
0.4
0.6
*
****
****
****
WT
RdRp tg/-
WT
RdRp tg/-
PBS Treated
BM12 Treated
B.
Germinal Center B cells
% FAS+ GL-7+ cells
0
2
4
6
8
****
****
****
****
***
WT
RdRp tg/-
WT
RdRp tg/-
PBS Treated
BM12 Treated
Plasma Cells
% CD19lo CD138+ cells
0
5
10
15
****
****
****
WT
RdRp tg/-
WT
RdRp tg/-
PBS Treated
BM12 Treated
C.
Tfh cells
% CCR5+ PD-1+ cells
0
1
2
3
4
5
****
**
**
WT
RdRp tg/-
WT
RdRp tg/-
PBS Treated
BM12 Treated
D.
anti-dsDNA antibodies
Concentration (µg/mL)
0
5
10
15
**
**
*
WT
RdRp tg/-
WT
RdRp tg/-
PBS Treated
BM12 Treated
anti-SmAg antibodies
Concentration (µg/mL)
0
50
100
150
200
250
**
**
WT
RdRp tg/-
WT
RdRp tg/-
PBS Treated
BM12 Treated
E.
Treg
%CD4+ FoxP3+ cells
10
12
14
16
18
****
WT
RdRp tg/-
Effector Treg
%CD62L- CD44+ cells
30
35
40
45
50
***
WT
RdRp tg/-
Naiive Treg
%CD62L+ CD44- cells
5
6
7
8
9
NS
WT
RdRp tg/-

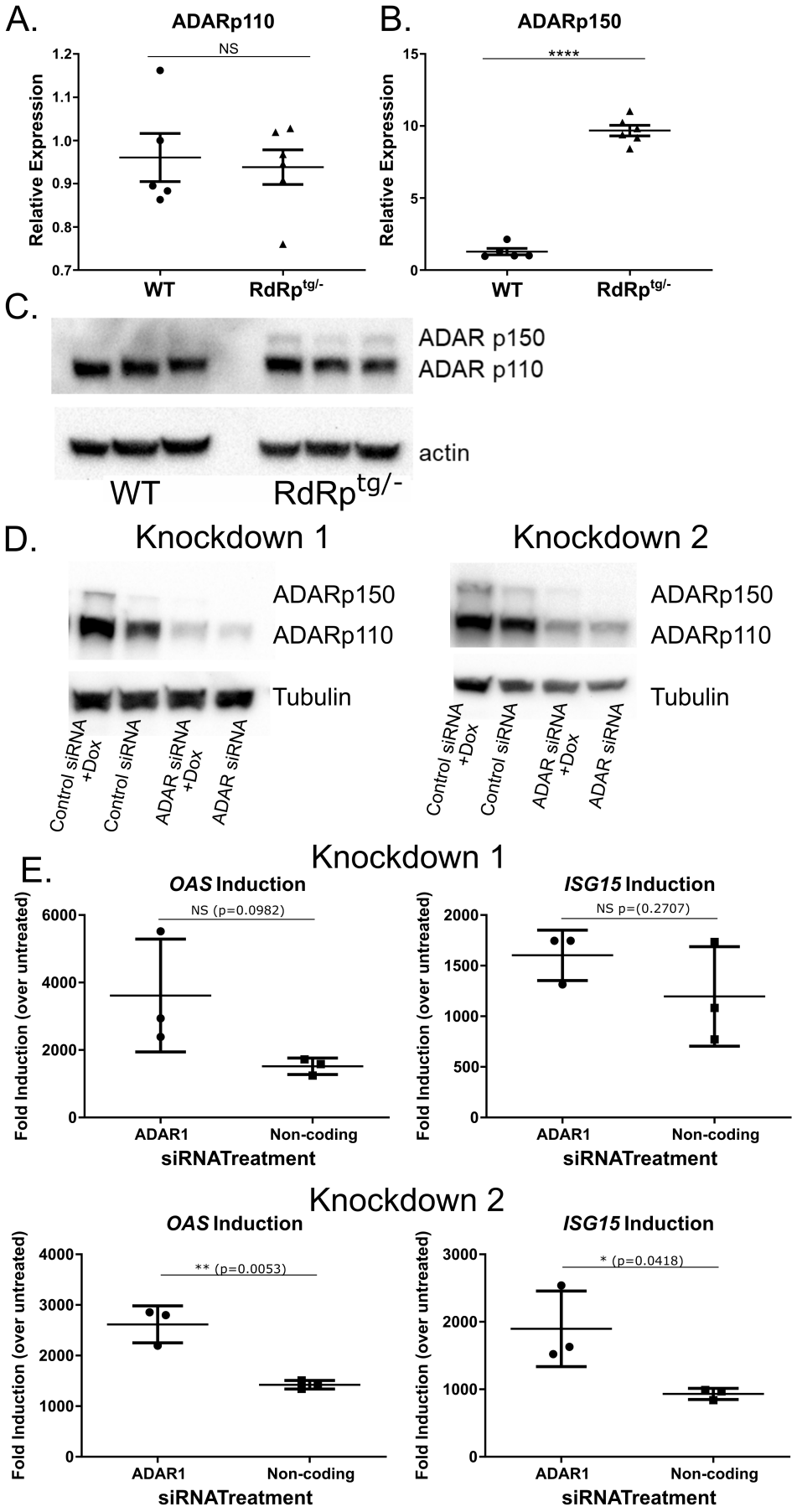
A.
ADARp110
NS
Relative Expression
1.2
1.1
1.0
0.9
0.8
0.7
WT
RdRp tg/-
B.
ADARp150
****
Relative Expression
15
10
5
0
WT
RdRp tg/-
C.
ADAR p150
ADAR p110
actin
WT
RdRp tg/-
D.
Knockdown 1
Knockdown 2
ADARp150
ADARp110
Tubulin
Control siRNA +Dox
Control siRNA
ADAR siRNA +Dox
ADAR siRNA
E.
Knockdown 1
OAS Induction
NS (p=0.0982)
ISG15 Induction
NS p=(0.2707)
Fold Induction (over untreated)
ADAR1
Non-coding
siRNATreatment
Knockdown 2
OAS Induction
** (p=0.0053)
ISG15 Induction
* (p=0.0418)

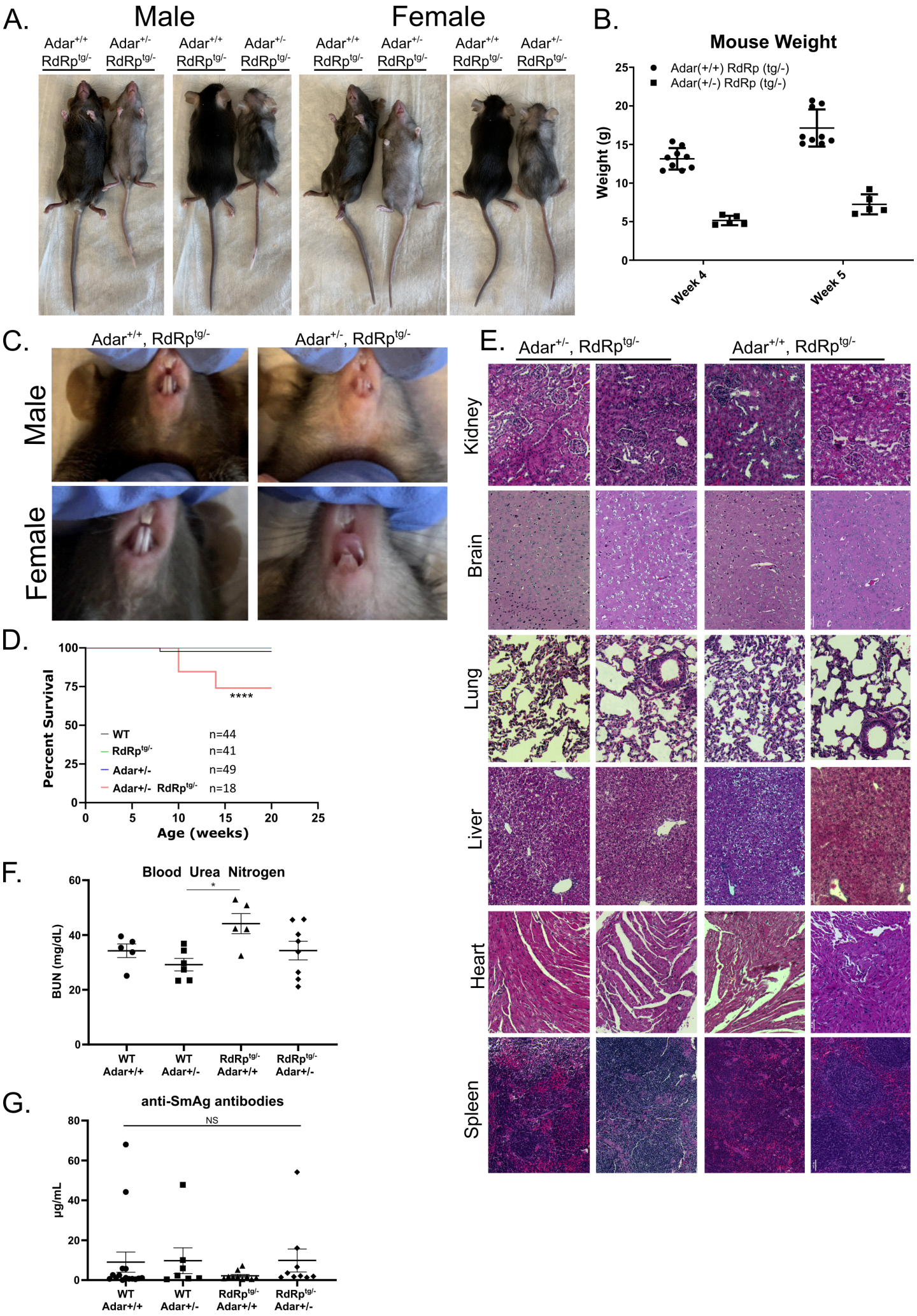
A.
Male
Female
Adar+/+ RdRptg/-
Adar+/- RdRptg/-
B.
Mouse Weight
Adar(+/+) RdRp (tg/-)
Adar(+/-) RdRp (tg/-)
Weight (g)
Week 4
Week 5
C.
Adar+/+, RdRptg/-
Adar+/-, RdRptg/-
Male
Female
D.
Percent Survival
Age (weeks)
****
WT n=44
RdRptg/- n=41
Adar+/- n=49
Adar+/- RdRptg/- n=18
E.
Adar+/-, RdRptg/-
Adar+/+, RdRptg/-
Kidney
Brain
Lung
Liver
Heart
Spleen
F.
Blood Urea Nitrogen
BUN (mg/dL)
*
WT Adar+/+
WT Adar+/-
RdRptg/- Adar+/+
RdRptg/- Adar+/-
G.
anti-SmAg antibodies
μg/mL
NS
WT Adar+/+
WT Adar+/-
RdRptg/- Adar+/+
RdRptg/- Adar+/-

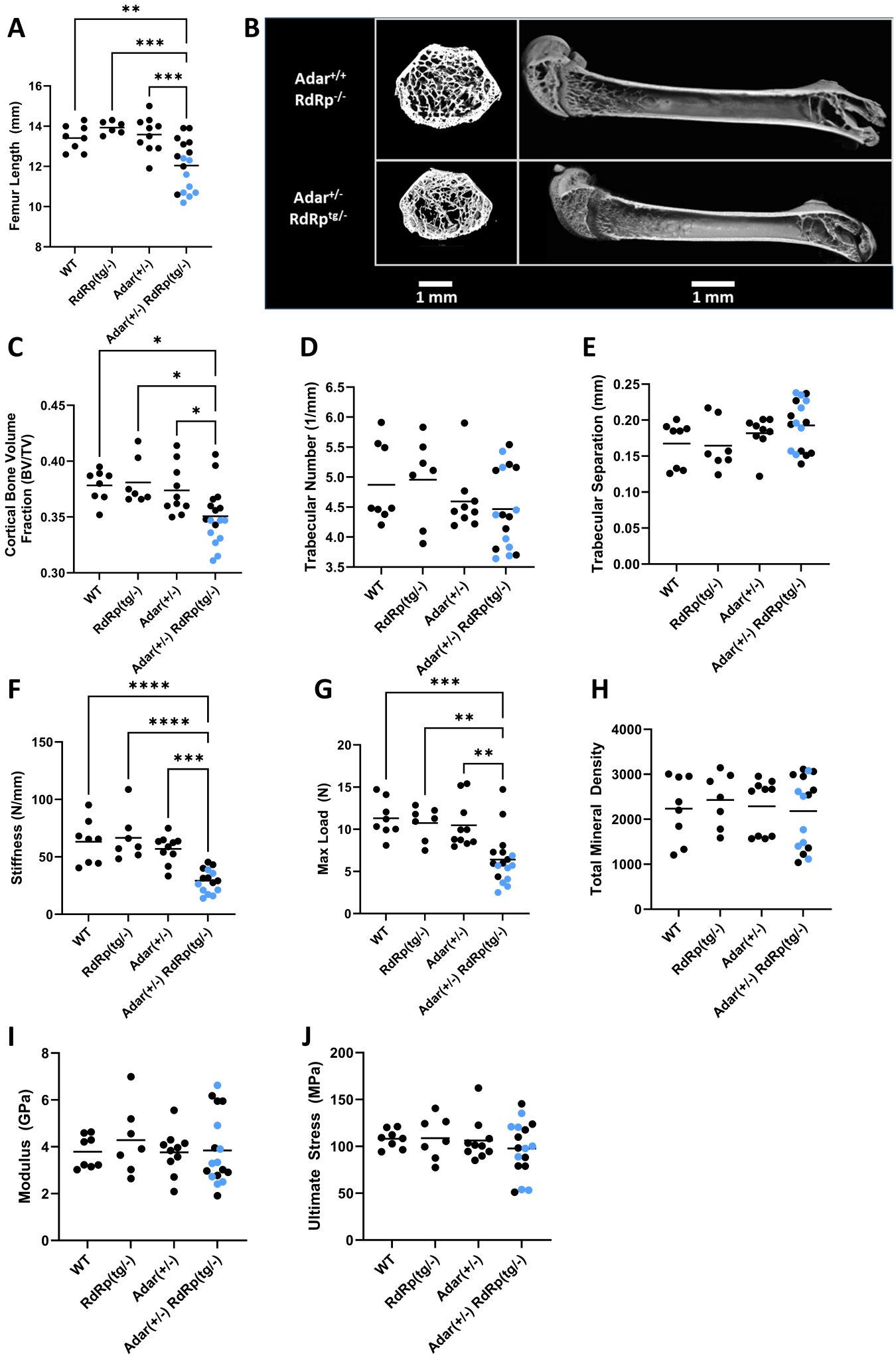
A
Femur Length (mm)
WT
RdRp(tg/-)
Adar(+/-)
Adar(+/-) RdRp(tg/-)
B
Adar+/+ RdRp-/-
Adar+/- RdRptg/-
1 mm
1 mm
C
Cortical Bone Volume Fraction (BV/TV)
D
Trabecular Number (1/mm)
E
Trabecular Separation (mm)
F
Stiffness (N/mm)
G
Max Load (N)
H
Total Mineral Density
I
Modulus (GPa)
J
Ultimate Stress (MPa)

Figure 4

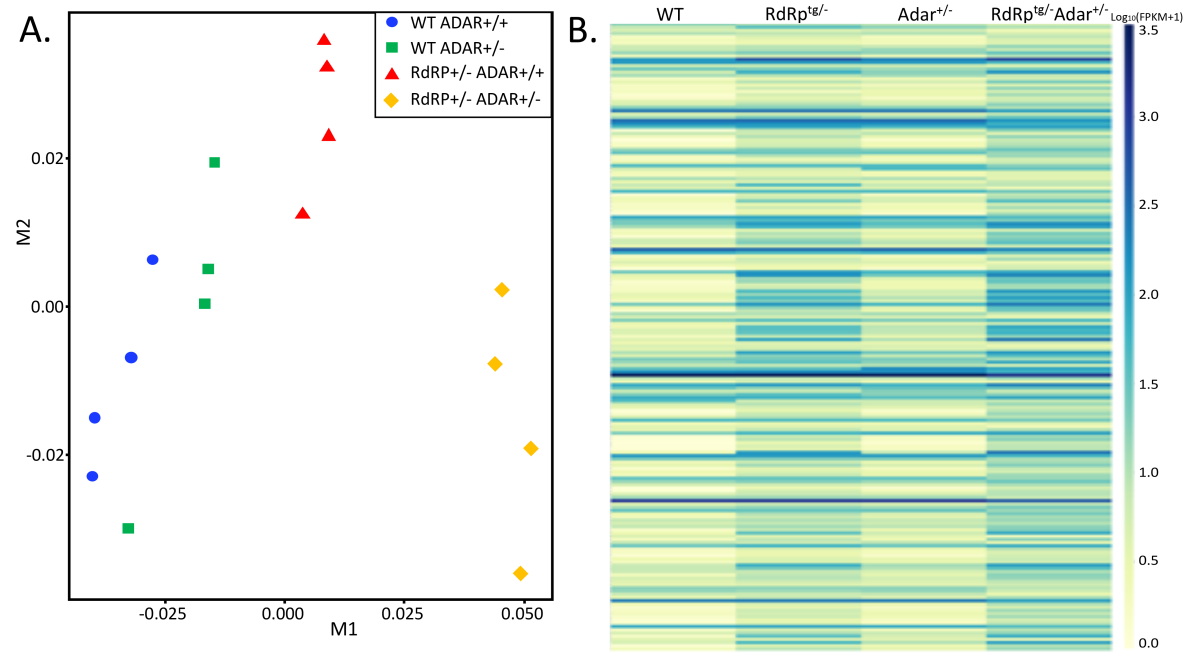

C.

Comparison	Up DEGs	Up ISGs (%)	Down DEGs	Down ISGs (%)	Total DEGs	Total ISGs (%)
WT vs. RdRp$^{tg/-}$	96	84 (87.5%)	6	2 (33.3%)	102	86 (84.3%)
WT vs. Adar$^{+/-}$	30	27 (90.0%)	5	3 (60.0%)	35	30 (85.7%)
WT vs. RdRp$^{tg/-}$Adar$^{+/-}$	151	136 (90.1%)	75	38 (50.7%)	226	174 (76.9%)
RdRp$^{tg/-}$ vs. Adar$^{+/-}$	6	4 (66.7%)	83	73 (87.9%)	89	77 (86.5%)
RdRp$^{tg/-}$ vs. RdRp$^{tg/-}$Adar$^{+/-}$	64	59 (92.2%)	67	35 (52.2%)	131	94 (71.8%)
Adar$^{+/-}$ vs. RdRp$^{tg/-}$Adar$^{+/-}$	137	124 (90.5%)	75	37 (49.3%)	212	161 (75.9%)

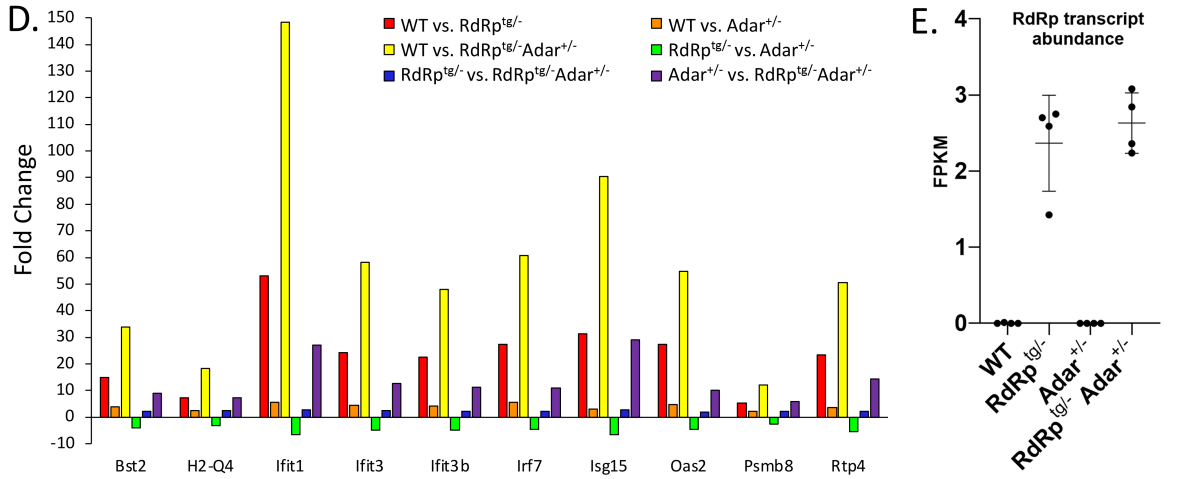

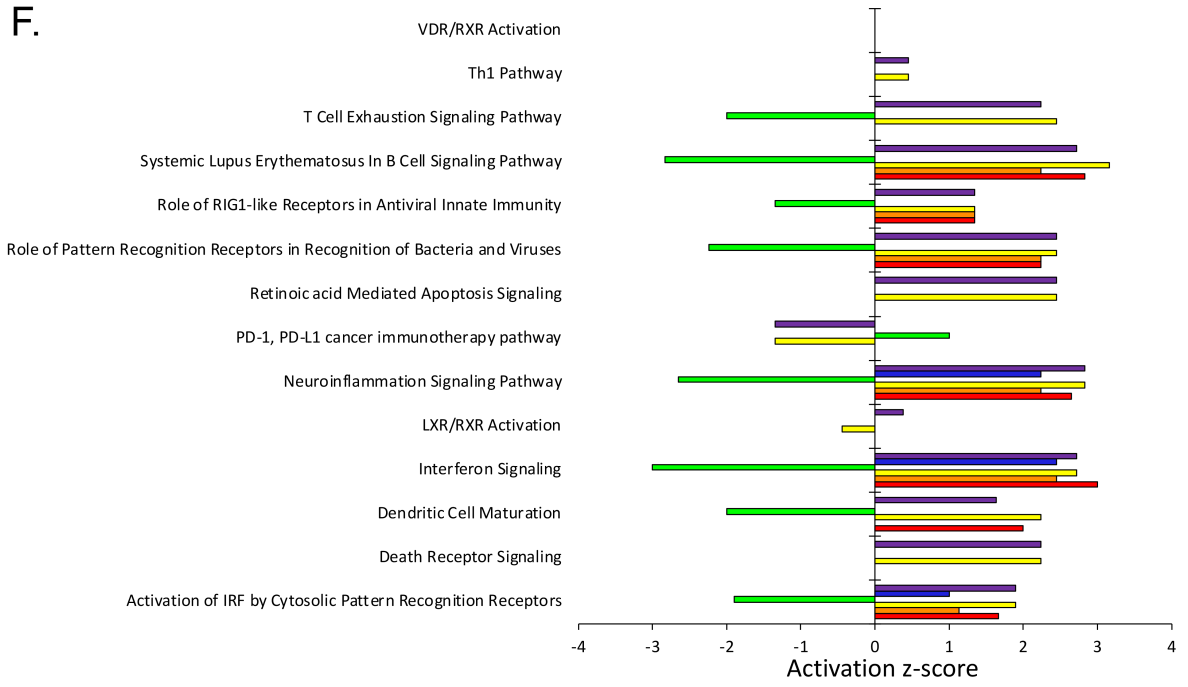

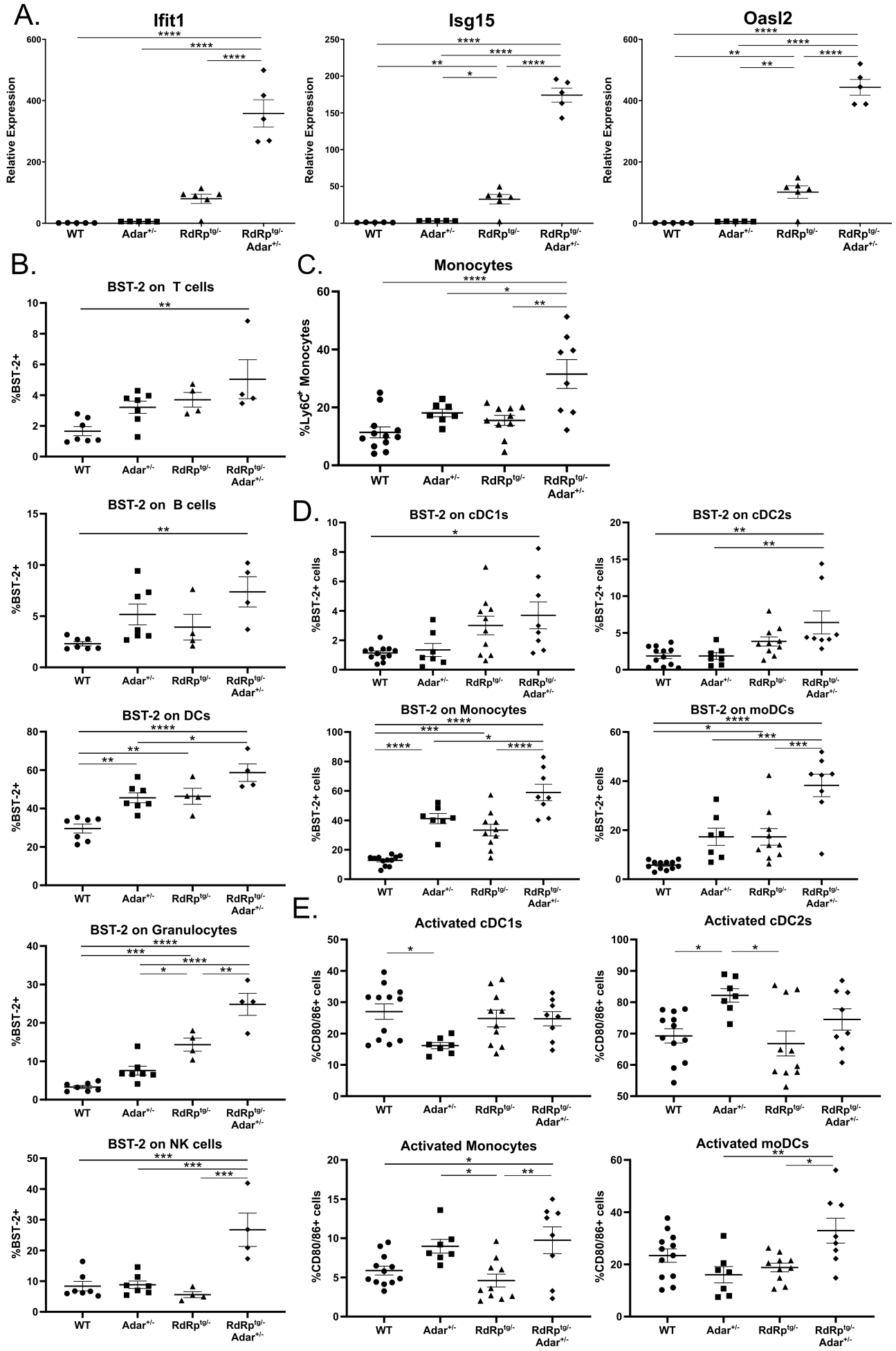
A.
Ifit1
Isg15
Oasl2
Relative Expression
WT
Adar+/-
RdRptg/-
RdRptg/- Adar+/-
B.
BST-2 on T cells
BST-2 on B cells
BST-2 on DCs
BST-2 on Granulocytes
BST-2 on NK cells
%BST-2+
C.
Monocytes
%Ly6C+ Monocytes
D.
BST-2 on cDC1s
BST-2 on cDC2s
BST-2 on Monocytes
BST-2 on moDCs
%BST-2+ cells
E.
Activated cDC1s
Activated cDC2s
Activated Monocytes
Activated moDCs
%CD80/86+ cells

A.

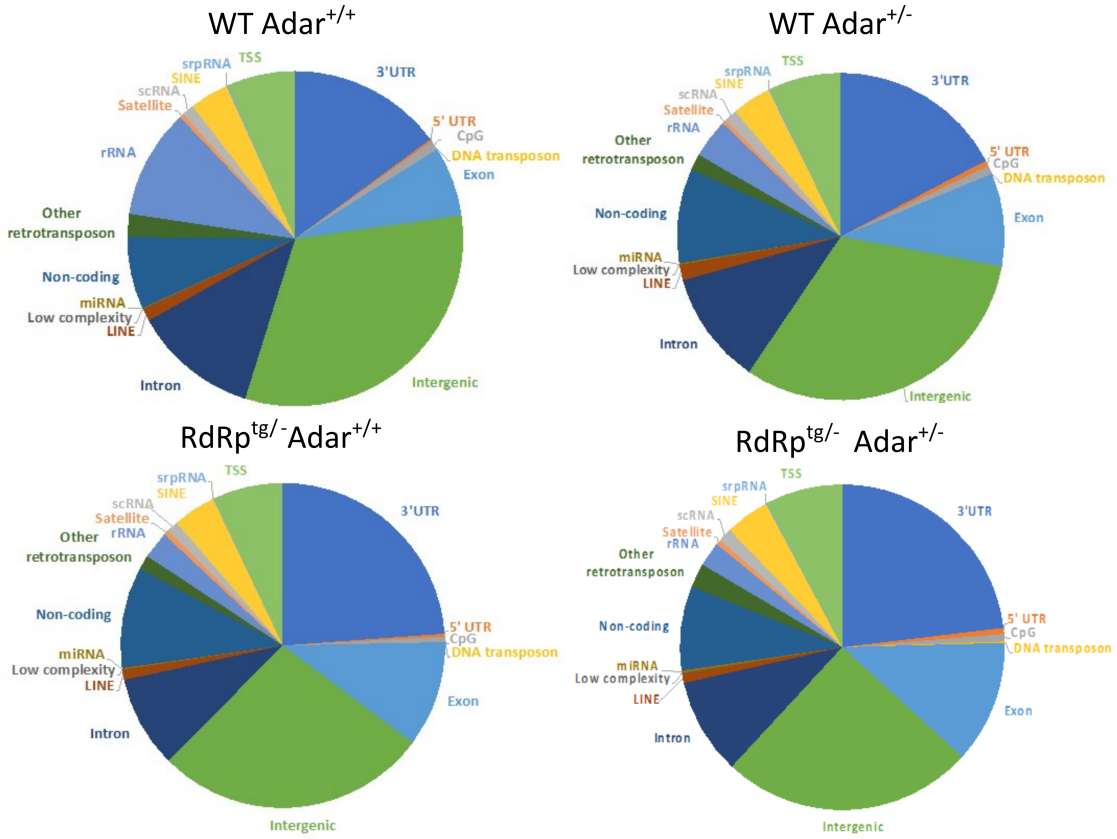

B.

	WT	RdRp$^{tg/-}$	Adar$^{+/-}$	RdRp$^{tg/-}$ Adar$^{+/-}$
Genes	2610	1989	2233	3077
Sites	1317	1446	1431	2174

Annotation	**WT**	**RdRp$^{tg/-}$**	**Adar$^{+/-}$**	**RdRp$^{tg/-}$ Adar$^{+/-}$**
3'UTR	210	344	247	500
5' UTR	3	4	8	13
CpG	13	8	12	16
DNA transposon	0	0	0	3
Exon	95	152	131	264
Intergenic	452	393	450	544
Intron	170	132	160	207
LINE	17	15	22	20
Low complexity	1	0	0	2
miRNA	1	2	2	5
Non-coding	98	145	133	181
Other retrotransposon	31	21	23	52
rRNA	149	39	55	53
Satellite	6	8	6	11
scRNA	16	16	18	30
SINE	53	62	55	95
srpRNA	2	1	2	2
TSS	93	101	102	167

C.

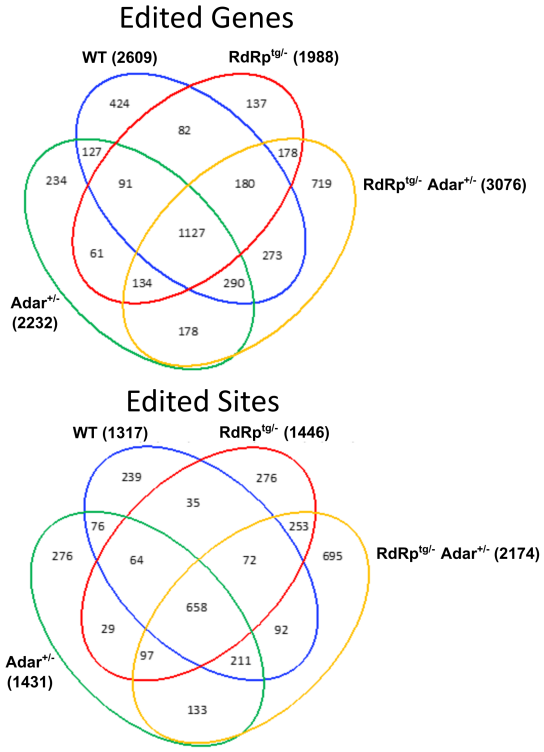

D.

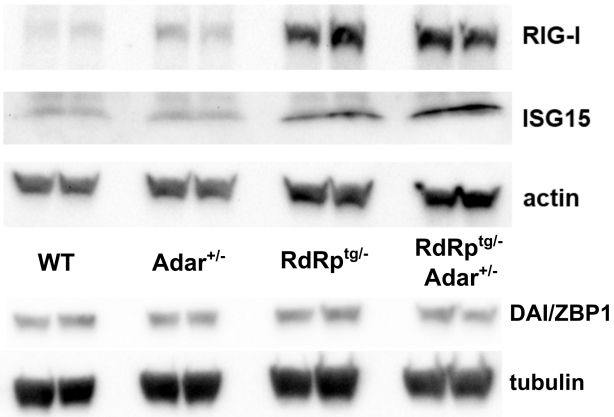

E.

RNAseq Expression Levels

	WT vs. Adar$^{+/-}$	WT vs. RdRp$^{tg/-}$	WT vs. RdRp$^{tg/-}$ Adar$^{+/-}$
RIG-I	ns	9.330	15.600
ISG15	3.099	31.218	90.325
ZBP1	2.919	4.013	5.471

F.

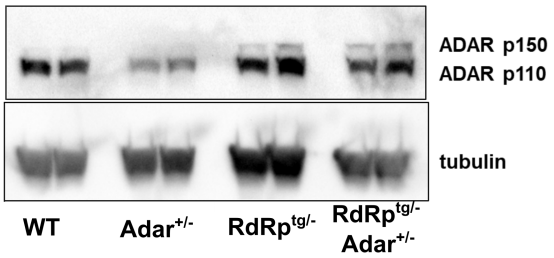

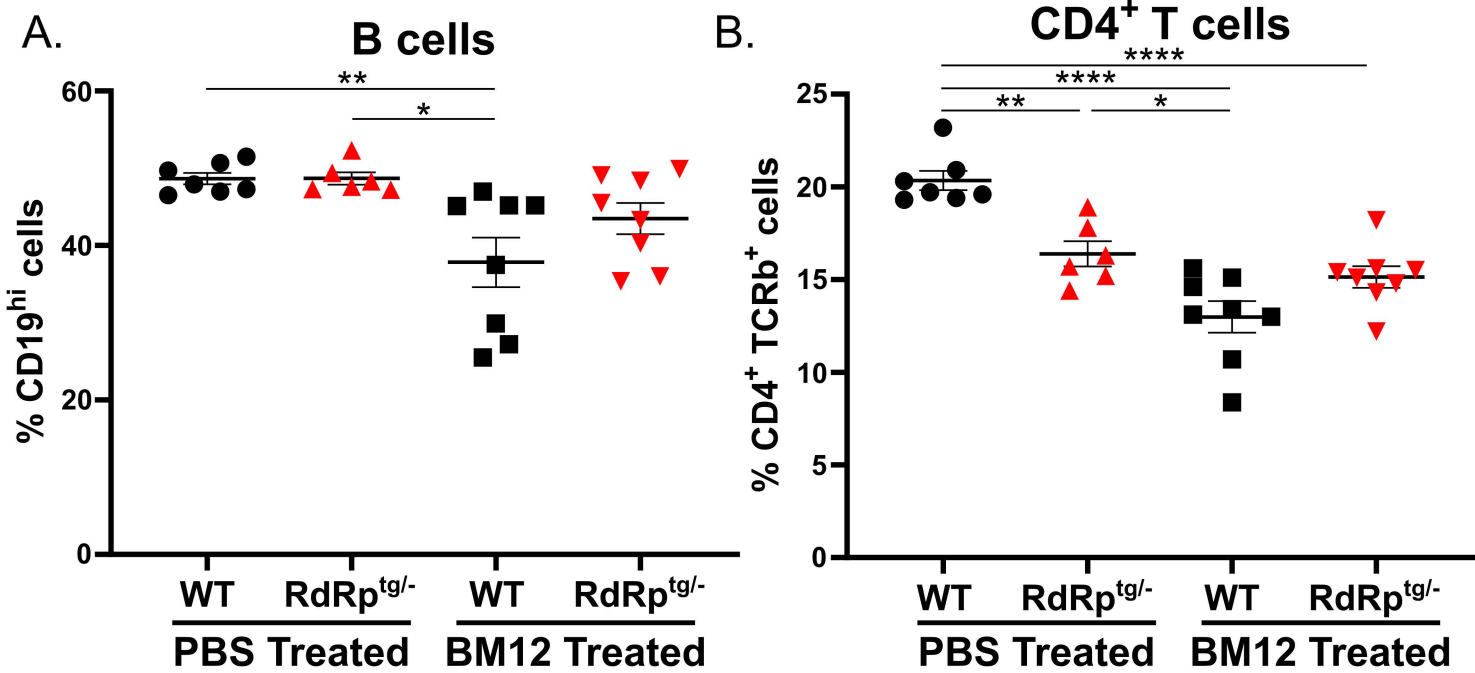

Supplemental Figure 1

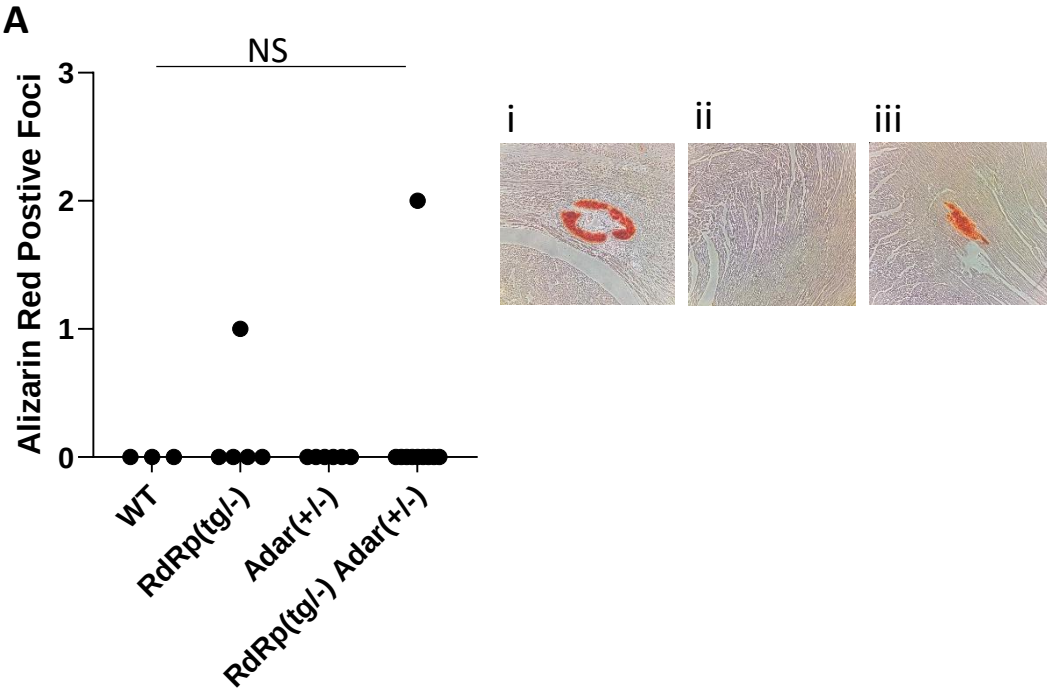

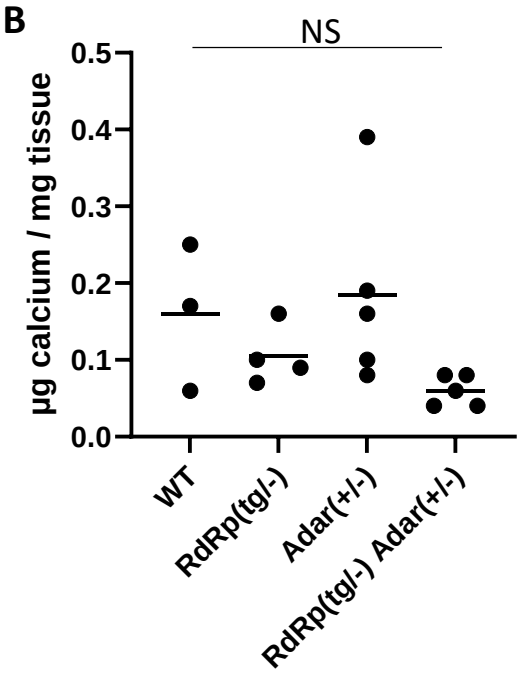

Supplemental Figure 2

Supplemental Figure 3

	WT vs. RdRP		WT vs. ADAR		WT vs. ADAR-RdRP		RdRP vs. ADAR		RdRP vs. ADAR-RdRP		ADAR vs. ADAR-RdRP	
Diseases or Functions Annotation	**-log(B-H p-value)**	**z-score**	**-log(B-H p-value)**	**z-score**	**-log(B-H p-value)**	**z-score**	**-log(B-H p-value)**	**z-score**	**-log(B-H p-value)**	**z-score**	**-log(B-H p-value)**	**z-score**
Antimicrobial response	0.00000	2.39	1.97E-09	1.455	NaN	NaN	0.00000	-2.39	1.08E-05	NaN	1.21E-12	0.995
Antiviral response	0.00000	2.39	2.77E-11	1.455	NaN	NaN	0.00000	-2.39	2.82E-06	NaN	6.75E-12	0.995
Apoptosis of breast cancer cell lines	NaN	NaN	NaN	NaN	NaN	NaN	NaN	NaN	NaN	NaN	0.00146	2.808
Apoptosis of epithelial cells	NaN	NaN	NaN	NaN	NaN	NaN	NaN	NaN	NaN	NaN	0.00003	2.55
Apoptosis of liver cells	NaN	NaN	NaN	NaN	NaN	NaN	NaN	NaN	NaN	NaN	0.00146	2.169
Cell death of epithelial cells	0.00251	2.414	NaN	NaN	NaN	NaN	NaN	NaN	1.06E-03	0.922	1.41E-05	3.058
Demyelination of nerves	NaN	NaN	NaN	NaN	NaN	NaN	NaN	NaN	0.00001	2.195	NaN	NaN
Differentiation of Th17 cells	NaN	NaN	NaN	NaN	NaN	NaN			NaN	NaN	0.00014	-2.382
Encephalitis	3.09E-04	-1.925	3.72E-07	0.264	NaN	NaN	NaN	NaN	1.09E-04	-1.361	0.00000	-3.488
Experimental autoimmune encephalomyelitis	5.09E-04	-1.639	7.57E-07	0.659	NaN	NaN	1.45E-06	1.881	1.66E-04	-1.37	0.00000	-3.326
Inflammation of absolute anatomical region	8.46E-06	-1.905	5.51E-08	-0.527	NaN	NaN	1.39E-07	1.365	0.00002	-2.537	0.00000	-3.351
Inflammation of organ	3.08E-05	-1.264	1.75E-07	0.255	NaN	NaN	1.71E-07	1.078	0.00001	-2.346	0.00000	-2.881
Inhibition of cells	NaN	NaN	NaN	NaN	NaN	NaN	NaN	NaN	NaN	NaN	0.00142	2.166
Maturation of phagocytes	NaN	NaN	2.29E-03	-0.169	NaN	NaN	0.00074	-2.183	NaN	NaN	5.47E-04	0.891
Necrosis	8.48E-03	1.117	NaN	NaN	NaN	NaN	NaN	NaN	0.00160	2.156	0.00004	2.291
Necrosis of epithelial tissue	NaN	NaN	NaN	NaN	NaN	NaN	NaN	NaN	1.36E-04	1.014	0.00000	2.072
Neuronal cell death	NaN	NaN	NaN	NaN	NaN	NaN	NaN	NaN	0.00476	2.302	0.00006	2.309
Proliferation of antigen presenting cells	NaN	NaN	NaN	NaN	NaN	NaN	2.26E-03	-0.865	3.64E-03	NaN	0.00014	2.201
Proliferation of blood cells	0.00421	2.084	NaN	NaN	NaN	NaN	NaN	NaN	9.98E-04	0.317	8.85E-06	0.535
Proliferation of immune cells	0.00429	2.084	NaN	NaN	NaN	NaN	NaN	NaN	9.14E-04	0.358	1.70E-05	0.808
Quantity of blood cells	0.00064	2.383	NaN	NaN	NaN	NaN	0.00193	-2.021	1.63E-04	0.487	2.79E-06	0.67
Quantity of IL-12 in blood	0.00002	-2	6.62E-03	NaN	NaN	NaN	0.00002	2	NaN	NaN	0.00007	-2
Quantity of interleukin	NaN	NaN	NaN	NaN	NaN	NaN	NaN	NaN	NaN	NaN	0.00064	-2
Quantity of leukocytes	0.00046	2.295	NaN	NaN	NaN	NaN	1.60E-03	-1.906	1.02E-04	0.167	9.96E-07	0.336
Quantity of phagocytes	0.00104	2.191	NaN	NaN	NaN	NaN	2.21E-03	-1.544	2.25E-05	-0.125	5.80E-05	-0.102
Quantity of protein in blood	0.00769	-2.909	NaN	NaN	NaN	NaN	0.00034	2.088	NaN	NaN	6.48E-04	-1.717
Rheumatic Disease	0.00000	-2.219	7.94E-05	-1	NaN	NaN	7.74E-07	1.179	3.07E-05	-0.503	2.99E-08	-1.157

Supplemental Figure 4

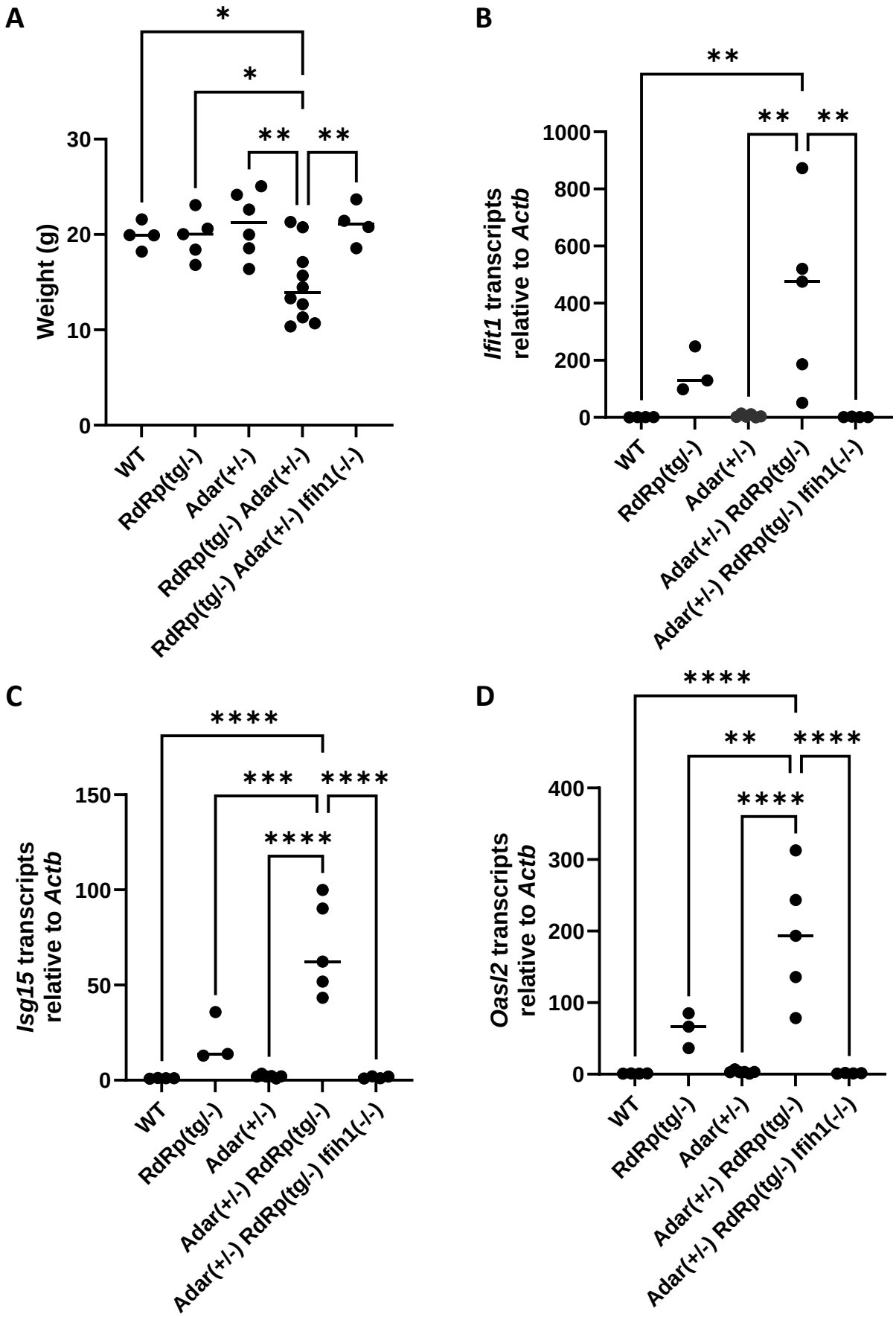

Supplemental Figure 5

Diseases or Functions Annotation	WT vs. RdRp$^{tg/-}$	WT vs. Adar$^{+/-}$	WT vs. RdRp$^{tg/-}$ Adar$^{+/-}$	RdRp$^{tg/-}$ vs. Adar$^{+/-}$	RdRp$^{tg/-}$ vs. RdRp$^{tg/-}$ Adar$^{+/-}$	Adar$^{+/-}$ vs. RdRp$^{tg/-}$ Adar$^{+/-}$
Activation of cells	2.339	1.88	2.069	-2.262	1.501	2.154
Activation of macrophages	1.803	1.282	2.145	-1.803	1.898	1.633
Activation of myeloid cells	1.472	0.943	2.084	-1.472	2.095	1.698
Activation of phagocytes	1.469	0.938	1.765	-1.469	2.095	1.795
Adhesion of blood cells	1.989	NA	2.637	NA	2.132	2.025
Antigen presentation	2.414	NA	2.414	NA	NA	2.414
Antigen presentation by cells	2	NA	2	NA	NA	2
Antimicrobial response	2.787	2.406	2.792	-2.947	NA	2.792
Antiviral response	2.787	2.406	2.792	-2.947	NA	2.792
Antiviral response of cells	2.219	1.982	1.31	-2.219	NA	1.31
Apoptosis	0.916	0.197	1.616	-0.696	1.157	2.443
Apoptosis of tumor cell lines	NA	NA	1.173	-0.889	NA	2.09
Autophagy of cells	2.072	NA	1.363	-1.502	1.095	1.152
Cell cycle progression	2.961	NA	2.195	-2.809	NA	2.448
Cell death of epithelial cells	NA	NA	1.966	NA	NA	2.68
Cell death of tumor cell lines	1.044	NA	1.396	-1.388	NA	2.158
Cell movement of leukocytes	2.904	NA	1.35	-2.394	1.501	1.387
Cell movement of monocytes	2.185	NA	2.083	NA	1.571	2.083
Cell movement of T lymphocytes	2.544	1.948	1.072	-1.824	1.645	1.072
Cellular homeostasis	1.314	1.026	2.089	-1.662	0.957	1.356
Cellular infiltration	2.619	NA	0.842	-1.692	1.402	1.042
Cellular infiltration by leukocytes	2.696	2.342	1.081	-2.13	1.481	1.294
Cellular infiltration by lymphocytes	2.187	NA	0.201	-1.507	0.692	0.201
Cellular infiltration by myeloid cells	1.878	2.091	0.83	NA	0.935	0.791
Contact growth inhibition	2.232	NA	2.467	-2.052	NA	2.467
Contact growth inhibition of tumor	NA	NA	2.022	-1.49	NA	2.022
Coordination	NA	NA	NA	NA	-2.401	NA
Cytostasis	2.442	NA	2.742	-2.522	NA	2.742
Cytostasis of tumor cell lines	1.972	1.451	NA	-1.762	NA	2.232
Cytotoxicity of cytotoxic T cells	2.439	NA	2.635	-1.988	NA	2.438
Cytotoxicity of lymphocytes	2.794	NA	2.605	-2.048	NA	2.412
Cytotoxicity of T lymphocytes	NA	NA	2.332	-1.583	NA	2.112
Degradation of DNA	NA	NA	2.781	NA	NA	2.781
Demyelination of nerves	NA	NA	1.798	NA	2.057	1.541
Differentiation of T lymphocytes	1.859	NA	1.227	-2.1	NA	0.815
Elimination of cells	NA	NA	2.2	NA	1.964	2.2
Encephalitis	-1.515	-1	-2.141	NA	-1.405	-2.141
Endocytosis	2.6	NA	NA	NA	NA	0.566
Fragmentation of DNA	NA	NA	2.598	NA	NA	2.598
Hematologic cancer	NA	NA	-2.752	NA	NA	-2.752
Hematologic cancer of cells	NA	NA	-2.396	NA	NA	-2.396
Hematopoietic neoplasm	NA	NA	-2.032	NA	NA	-2.032
Immune response of brain	-1.745	NA	-2.311	1.992	NA	-2.311
Immune response of cells	3.924	3.1	2.981	-3.066	NA	2.445
Immune response of leukocytes	2.415	1.981	0.755	-1.218	1.004	0.08
Infection by Flaviviridae	-1.732	-1.732	-2	1.732	NA	-2
Infection by Herpesviridae	NA	NA	-2.187	NA	NA	-2.187
Infection by RNA virus	-1.879	-2.019	-2.719	2.088	-1.388	-2.745
Infection of cells	-1.152	NA	-2.341	1.417	-1.2	-2.371
Infection of kidney cell lines	-1.651	-1.337	-2.093	1.651	NA	-2.291
Infection of mammalia	-3.48	-2.662	-3.452	3.388	-1.445	-3.207
Infiltration by T lymphocytes	2.187	NA	0.052	-1.507	0.842	0.052
Inflammation of absolute anatomic	-1.386	-0.851	-2.132	1.358	-0.958	-2.132
Inflammation of organ	-1.311	-0.729	-2.222	1.29	-0.76	-2.173
Inhibition of lymphocytes	NA	NA	2.172	NA	NA	2.172
Inhibition of RNA virus	1.974	NA	2.196	-1.974	NA	1.568
Inhibition of virus	NA	NA	2.415	-2.211	NA	1.848
Innate immune response	2.63	2.219	3.43	-3.132	2.8	3.43
Leukocyte migration	2.991	NA	1.565	-2.488	1.505	1.326
Lymphatic system tumor	NA	NA	-2.592	NA	NA	-2.592
Lymphocyte migration	2.721	2.144	0.753	-2.044	1.211	0.753
Lymphocytic cancer	NA	NA	-2.593	NA	NA	-2.593
Lymphocytic neoplasm	NA	NA	-2.593	NA	NA	-2.593
Lymphohematopoietic cancer	NA	NA	-2.752	NA	NA	-2.752
Lymphohematopoietic neoplasia	NA	NA	-2.032	NA	NA	-2.032
Lymphoid cancer	NA	NA	-2.593	NA	NA	-2.593
Lymphoreticular neoplasm	NA	NA	-2.4	NA	NA	-2.4
Migration of cancer cells	1.342	2	0.213	-1.342	0.956	0.508
Migration of cells	3.179	2.898	1.999	-2.573	0.825	1.285
Morbidity or mortality	-2.789	NA	-1.199	NA	0.575	-0.651
Necrosis	1.494	1.476	2.39	-1.714	2.274	2.989
Necrosis of epithelial tissue	NA	NA	1.737	NA	NA	2.346
Neoplasia of blood cells	NA	NA	-2.512	NA	NA	-2.512
Neoplasia of leukocytes	NA	NA	-2.396	NA	NA	-2.396
Neuromuscular disease	2.219	1.982	1.664	-1.982	1.387	1.664
Polarization of blood cells	NA	NA	NA	NA	2	NA
Polarization of cells	NA	1.982	NA	NA	2.219	NA
Production of protein	1.53	1.217	1.148	-2.096	0.485	0.678
Quantity of blood cells	2.217	1.36	0.079	-2.117	0.041	0.653
Quantity of CD8+ T lymphocyte	2.388	2.191	1.721	-2.207	1.461	1.721
Quantity of cytokine	NA	NA	-2.343	NA	NA	-2.154
Quantity of IFNG in blood	-2.183	NA	-2.4	2.183	NA	-2.4
Quantity of MHC Class I on cell surf	2.207	NA	2.207	-1.981	NA	2.207
Recruitment of leukocytes	2.339	2.339	2.156	-1.666	1.812	1.089
Recruitment of T lymphocytes	1.96	1.96	2.199	-1.96	1.996	NA
Replication of Flaviviridae	-2.643	-2.643	-2.988	2.826	-2.275	-2.988
Replication of flavivirus	-1.963	-2.181	-2.181	2.181	-1.939	-2.181
Replication of Hepatitis C virus	-2.335	-2.111	-2.528	2.324	NA	-2.528
Replication of Herpesviridae	-2.132	-2.828	-3.175	2.525	-2.236	-3.175
Replication of Murine herpesvirus 4	-2.236	-2	-2.828	2.236	NA	-2.828
Replication of RNA virus	-2.875	-3.077	-3.617	3.292	-2.304	-3.497
Replication of vesicular stomatitis v	-2.679	-2.473	-3.129	2.841	-1.702	-3.129
Replication of viral replicon	-2.818	-3.115	-3.56	3.271	-2.782	-3.56
Replication of virus	-3.082	-3.443	-3.924	3.583	-2.607	-3.812
Response of antigen presenting cel	2.219	NA	1.65	NA	NA	0.799
Response of embryonic cell lines	1.96	NA	2.4	-2.2	NA	2.4
Response of epithelial cell lines	1.969	NA	2.404	-2.207	NA	2.404
Response of kidney cell lines	1.969	NA	2.404	-2.207	NA	2.404
Response of phagocytes	2.207	2.207	NA	-2.207	NA	0.845
Transactivation of RNA	NA	1.961	NA	-2.41	NA	NA
Viral Infection	-3.615	-3.851	-4.1	3.801	-2.583	-3.943
Viral life cycle	NA	NA	-3.683	NA	NA	-3.683

Supplemental Figure 6

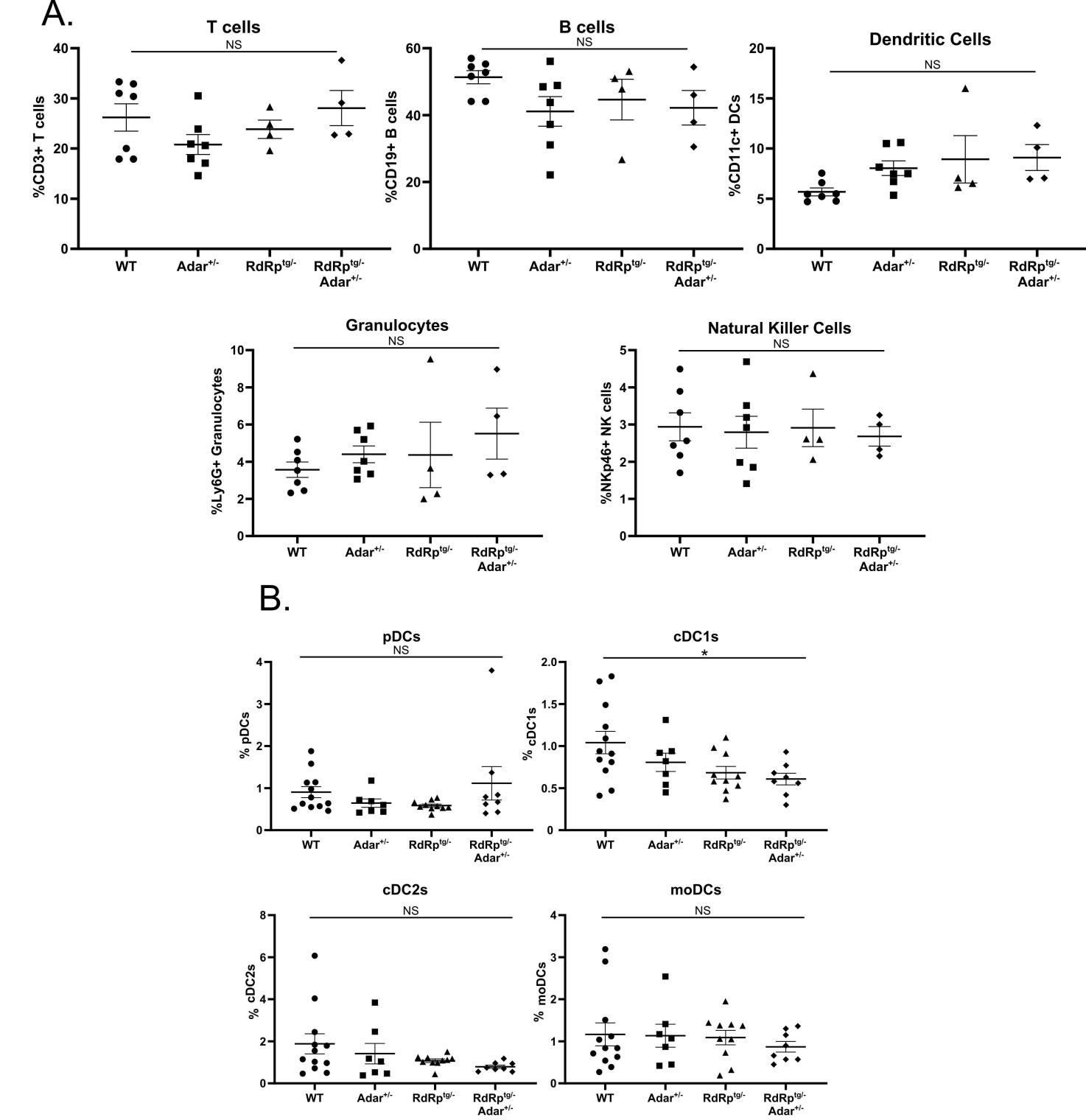

Supplemental Figure 7

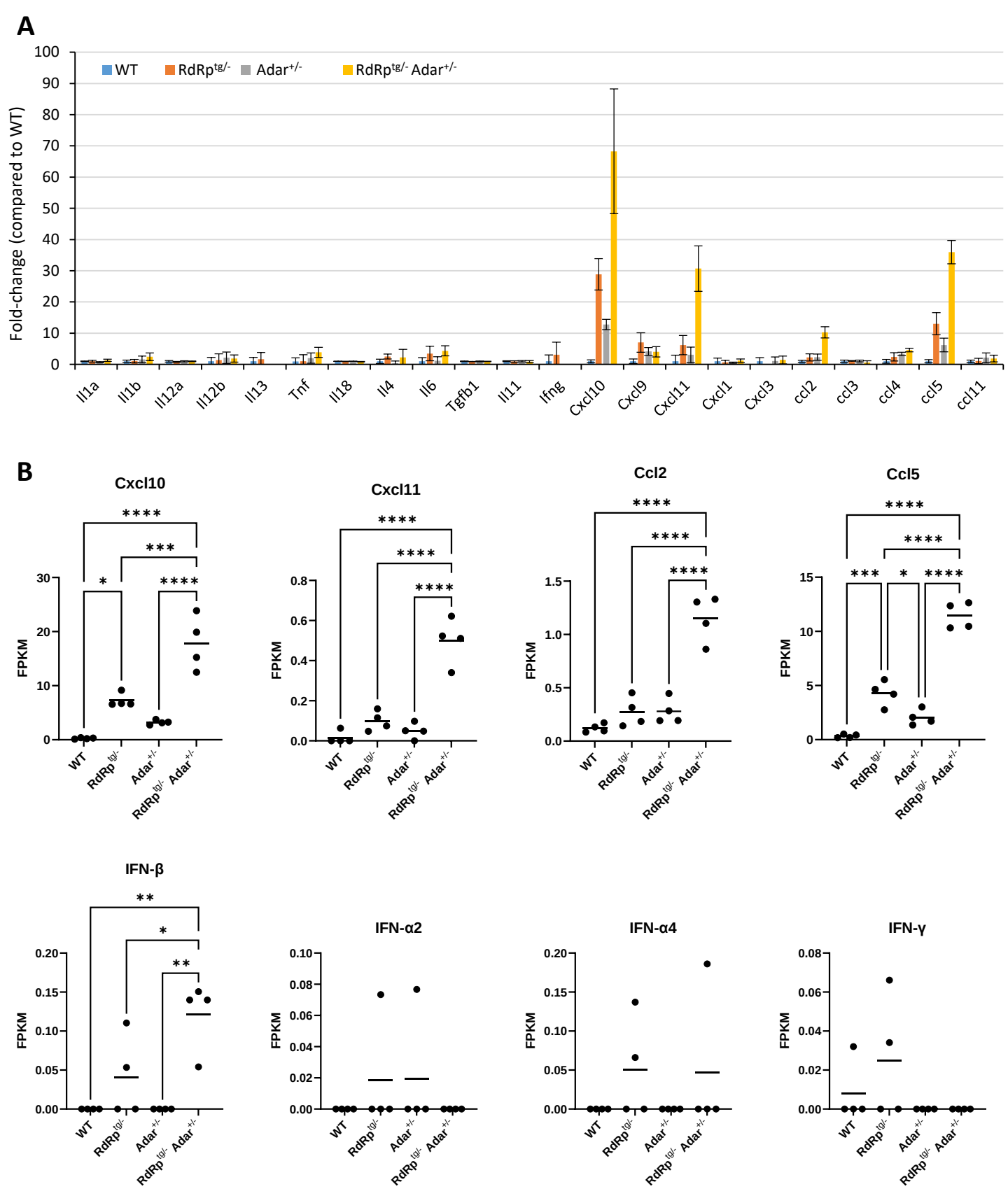

Supplemental Figure 8

	WT vs. RdRp$^{tg/-}$		WT vs. Adar$^{+/-}$		WT vs. RdRp$^{tg/-}$ Adar$^{+/-}$		RdRp$^{tg/-}$ vs. Adar$^{+/-}$		RdRp$^{tg/-}$ vs. Adar$^{+/-}$ RdRp$^{tg/-}$		Adar$^{+/-}$ vs. Adar$^{+/-}$ RdRp$^{tg/-}$	
Diseases or Functions Annotation	**-log(B-H p-value)**	**z-score**	**-log(B-H p-value)**	**z-score**	**-log(B-H p-value)**	**z-score**	**-log(B-H p-value)**	**z-score**	**-log(B-H p-value)**	**z-score**	**-log(B-H p-value)**	**z-score**
Antimicrobial response	0.00000	2.39	1.97E-09	1.455	NaN	NaN	0.00000	-2.39	1.08E-05	NaN	1.21E-12	0.995
Antiviral response	0.00000	2.39	2.77E-11	1.455	NaN	NaN	0.00000	-2.39	2.82E-06	NaN	6.75E-12	0.995
Apoptosis of breast cancer cell lines	NaN	NaN	NaN	NaN	NaN	NaN	NaN	NaN	NaN	NaN	0.00146	2.808
Apoptosis of epithelial cells	NaN	NaN	NaN	NaN	NaN	NaN	NaN	NaN	NaN	NaN	0.00003	2.55
Apoptosis of liver cells	NaN	NaN	NaN	NaN	NaN	NaN	NaN	NaN	NaN	NaN	0.00146	2.169
Cell death of epithelial cells	0.00251	2.414	NaN	NaN	NaN	NaN	NaN	NaN	1.06E-03	0.922	1.41E-05	3.058
Demyelination of nerves	NaN	NaN	NaN	NaN	NaN	NaN	NaN	NaN	0.00001	2.195	NaN	NaN
Differentiation of Th17 cells	NaN	NaN	NaN	NaN	NaN	NaN			NaN	NaN	0.00014	-2.382
Encephalitis	3.09E-04	-1.925	3.72E-07	0.264	NaN	NaN	NaN	NaN	1.09E-04	-1.361	0.00000	-3.488
Experimental autoimmune encephalomyelitis	5.09E-04	-1.639	7.57E-07	0.659	NaN	NaN	1.45E-06	1.881	1.66E-04	-1.37	0.00000	-3.326
Inflammation of absolute anatomical region	8.46E-06	-1.905	5.51E-08	-0.527	NaN	NaN	1.39E-07	1.365	0.00002	-2.537	0.00000	-3.351
Inflammation of organ	3.08E-05	-1.264	1.75E-07	0.255	NaN	NaN	1.71E-07	1.078	0.00001	-2.346	0.00000	-2.881
Inhibition of cells	NaN	NaN	NaN	NaN	NaN	NaN	NaN	NaN	NaN	NaN	0.00142	2.166
Maturation of phagocytes	NaN	NaN	2.29E-03	-0.169	NaN	NaN	0.00074	-2.183	NaN	NaN	5.47E-04	0.891
Necrosis	8.48E-03	1.117	NaN	NaN	NaN	NaN	NaN	NaN	0.00160	2.156	0.00004	2.291
Necrosis of epithelial tissue	NaN	NaN	NaN	NaN	NaN	NaN	NaN	NaN	1.36E-04	1.014	0.00000	2.072
Neuronal cell death	NaN	NaN	NaN	NaN	NaN	NaN	NaN	NaN	0.00476	2.302	0.00006	2.309
Proliferation of antigen presenting cells	NaN	NaN	NaN	NaN	NaN	NaN	2.26E-03	-0.865	3.64E-03	NaN	0.00014	2.201
Proliferation of blood cells	0.00421	2.084	NaN	NaN	NaN	NaN	NaN	NaN	9.98E-04	0.317	8.85E-06	0.535
Proliferation of immune cells	0.00429	2.084	NaN	NaN	NaN	NaN	NaN	NaN	9.14E-04	0.358	1.70E-05	0.808
Quantity of blood cells	0.00064	2.383	NaN	NaN	NaN	NaN	0.00193	-2.021	1.63E-04	0.487	2.79E-06	0.67
Quantity of IL-12 in blood	0.00002	-2	6.62E-03	NaN	NaN	NaN	0.00002	2	NaN	NaN	0.00007	-2
Quantity of interleukin	NaN	NaN	NaN	NaN	NaN	NaN	NaN	NaN	NaN	NaN	0.00064	-2
Quantity of leukocytes	0.00046	2.295	NaN	NaN	NaN	NaN	1.60E-03	-1.906	1.02E-04	0.167	9.96E-07	0.336
Quantity of phagocytes	0.00104	2.191	NaN	NaN	NaN	NaN	2.21E-03	-1.544	2.25E-05	-0.125	5.80E-05	-0.102
Quantity of protein in blood	0.00769	-2.909	NaN	NaN	NaN	NaN	0.00034	2.088	NaN	NaN	6.48E-04	-1.717
Rheumatic Disease	0.00000	-2.219	7.94E-05	-1	NaN	NaN	7.74E-07	1.179	3.07E-05	-0.503	2.99E-08	-1.157

Supplemental Figure 9

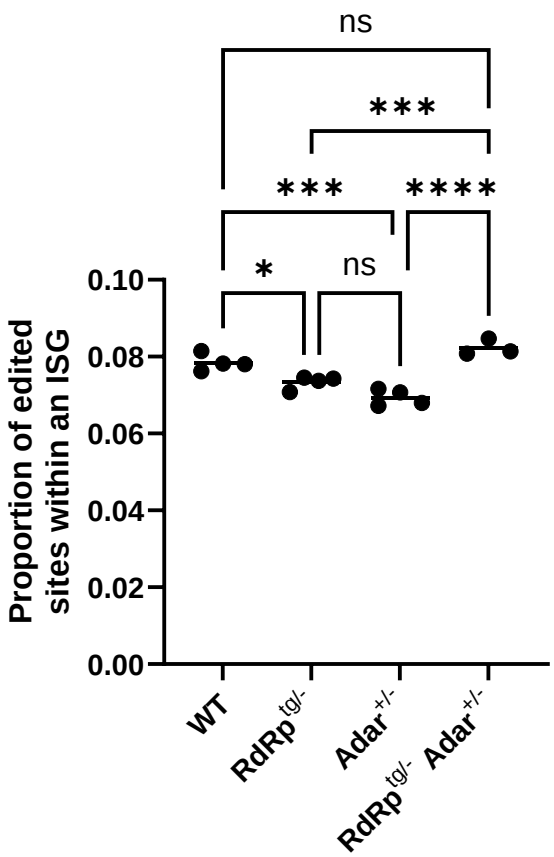

Supplemental Figure 10

Supplemental Figure Legends

Fig. S1. Overall B cell and T cell populations are marginally changed during BM12 transfer. Single cell, RBC-lysed splenocyte suspensions were made from sham or BM12 transferred animals for flow cytometry analysis. **(A)** Overall B cell populations in animals as defined by cd19 expression. **(B)** Overall $CD4^+$ T cell population in the spleens of experimental animals, as defined by TCRβ and CD4 expression. Data were analyzed using a one-way ANOVA followed by a Tukey tests where * = $p < 0.05$, ** = $p < 0.01$, *** = $p < 0.001$, **** = $p < 0.0001$. n = 7, 6, 8, 8 for WT (PBS), *RdRp*$^{tg/-}$ (PBS), WT (BM12), and *RdRp*$^{tg/-}$ (BM12), respectively. Data represent individual animals with the mean and s.d. shown as bars.

Fig. S2. Analysis of organ calcification. Flash frozen brain and formalin-fixed paraffin embedded heart were collected from 6-week-old mice. **(A)** Heart samples were stained with Alizarin Red and calcium depositions were manually counted and shown as Alizarin Red foci per animal (n = 3, 5, 5, 10 for WT, *Adar*$^{+/-}$, *RdRp*$^{tg/}$, *RdRp*$^{tg/-}$ *Adar*$^{+/-}$, respectively). Representative heart section images are shown to the right: (i) positive control heart provided by UCDSOM Research Histology Core Laboratory; (ii) RdRp$^{tg/-}$ Adar$^{+/-}$ heart without Alizarin red foci; (iii) RdRp$^{tg/-}$ Adar$^{+/-}$ heart with a positive focus. **(B)** Calcium was quantified from brain tissues (n = 3, 4, 5, 5). Data were analyzed using a one-way ANOVA followed by a Tukey tests; there were no significant differences between the groups. ns: not significant.

Fig. S3. Heatmap of differentially expressed ISGs across the four genotypes. Enlarged image of Fig. 5B with gene names displayed. FPKM values were log transformed with 1 pseudocount to facilitate visualization.

Fig. S4. Predicted upstream regulators. Predicted upstream signaling regulators as determined by IPA in various genotype comparisons between WT, *Adar*$^{+/-}$, *RdRp*$^{tg/-}$, and *Adar*$^{+/-}$ *RdRp*$^{tg/-}$ mice where red/green indicates whether the gene itself is upregulated/downregulated in the RNA-seq and orange/blue indicates predicated activation/inhibition of the molecular pathway it regulates.

Fig. S5. Loss of MDA5 rescues runting phenotype and abolished ISG upregulation. 6-week-old animals were weighed **(A)** and RNA was isolated from whole-brains for qPCR analysis of the ISGs Ifit1 **(B)**, Isg15 **(C)**, and Oasl2 **(D)**. Data were analyzed using a one-way ANOVA followed by a Tukey tests where * = $p < 0.05$, ** = $p < 0.01$, *** = $p < 0.001$, **** = $p < 0.0001$. For (A), n = 4, 5, 6, 10, and 4 for WT, *Adar*$^{+/-}$, *RdRp*$^{tg/}$, *RdRp*$^{tg/-}$ *Adar*$^{+/-}$, and *RdRp*$^{tg/-}$ *Adar*$^{+/-}$ *Ifih1*$^{-/-}$, respectively. For (B-D), n = 4, 3, 5, 5, and 4. Data points represent individual animals with the mean for each group shown as a bar.

Fig. S6. Disease and Biological Functions. Enriched diseases and biological functions across comparisons of gene expression changed between WT, *Adar*$^{+/-}$, *RdRp*$^{tg/-}$, and *Adar*$^{+/-}$ *RdRp*$^{tg/-}$ mice. Orange indicated that the disease or biological function is predicted to be enriched for and blue indicated is predicted to be inhibited.

Fig. S7. Certain immune cell populations are unchanged in *RdRp*$^{tg/-}$ *Adar*$^{+/-}$ mice. Splenocytes from 4-5 week old mice were harvested and single cell, RBC-lsysed solutions were made for FACS analysis. **(A)** T cells, B cells, DCs, granulocytes, and NK cells show no difference across groups measured. n = 7, 7, 4, and 4 for WT, *Adar*$^{+/-}$, *RdRp*$^{tg/}$, and *RdRp*$^{tg/-}$ *Adar*$^{+/-}$, respectively. **(B)** DC subsets including pDCs, cDC1s, cDC2s, and moDCs show minor or no difference in populations across groups. n = 12, 7, 10, and 8 for WT, *Adar*$^{+/-}$, *RdRp*$^{tg/}$, and *RdRp*$^{tg/-}$ *Adar*$^{+/-}$, respectively. ll data was analyzed using a one-way ANOVA followed by a Tukey

test to determine significance. * = $p < 0.05$. Data represent individual animals, graphs show means and s.d.

Fig. S8. Chemokine, cytokine and IFN expression changes. (A) RNA-seq-derived gene expression changes were determined for chemokines and cytokines and are shown as the average fold-change compared to wild-type mice, +/- s.d. **(B)** Individual animal FPKM values for cxcl10, cxcl11, ccl2, ccl5, IFN-β, IFN-α2, IFN-α4, and IFN-γ were graphed separately. Data were analyzed using a one-way ANOVA followed by a Tukey test to determine significance. No significant changes were observed for IFN-α2, IFN-α4, and IFN-γ. * = $p < 0.05$, ** = $p < 0.01$, *** = $p < 0.001$, **** = $p < 0.0001$.

Fig. S9. Diseases and Biological Functions enriched for in A-to-I edited genes. Genes with A-to-I edit sites and RNA-seq-derived expression changes were analyzed using IPA to determine enriched diseases and biological functions across genotype comparisons (WT, *Adar*$^{+/-}$, *RdRp*$^{tg/-}$, and *Adar*$^{+/-}$ *RdRp*$^{tg/-}$). Orange indicates that the disease or biological function is predicted to be enriched for or activated and blue indicates is predicted to be inhibited.

Fig. S10. Proportion of edited sites in ISG RNAs as a fraction of all uniquely edited sites per animal. Sites of A-to-I editing that were within an ISG were identified and the proportion of ISG edited sites out of all unique edited sites per animal was calculated. Bars indicate group means, dots represent individual animals, and the error bars are s.d. Data were analyzed using a one-way ANOVA followed by a Tukey tests where * = $p < 0.05$, *** = $p < 0.001$, **** = $p < 0.0001$, ns = not significant.

Supplemental Methods, Miller et al.

PCR primers and antibodies

a. Primers

Mus musculus

Gapdh: 5'-CATGGCCTTCCGTGTTCCTA-3' & 5'-CTATGTTTCCCGCGGCACGTCAGATCCA-3'
Ifit1: 5'-TTTGTTGTTGTTGTTGTTCGTT-3' & 5'-GCAGGAATCAGTTGTGATCT-3'
ISG15: 5'- TGGTACAGAACTGCAGCGAG -3' & 5'- CAGCCAGAACTGGTCTTCGT -3'
Oasl2: 5'-CAAACAAACAAACAAACCCTCTC-3' & 5'-TCAAGGTGTCACTCTGCAT-3'
Adar p150 5'-GGCCTTGCCGGCACTATGTCTC-3' & 5' GCGGGTATCTCCACTTGCTATGCTC-3'
Adar p110: 5'-GGTGGAAGACTACGCGTTGGGAC-3' & 5' ACGACTGTGTCTGGTGAGGGAACAC-3'
IFNβ: 5'-CACAGCCCTCTCCATCAACTATAAGCAG-3'& 5'-CTGTAGGTGAGGTTGATCTTTCCATTCAG-3'

Homo sapiens

GAPDH: 5'-TGGACCTGACCTGCCGT-3' & 5'-TGGAGGAGTGGGTGTCGC-3'
ISG15: 5'-GTGGACAAATGCGACGAACC-3' & 5'-ATTTCCGGCCCTTGATCCTG-3'
OASL: 5'-GGATCTTCTCCCACACTCACATCT-3' & 5'-CACCATCAGGATTCTTCACGAA-3'

b. Antibodies

Rabbit polyclonal anti-ADAR1 (1:1,000 dilution; Cell Signaling, 14175)
Mouse anti-tubulin (1:5,000 dilution; Sigma, T5168)
Rabbit anti-Rig-I: mouse tissue blots (1:1,000 dilution, Cell Signaling, 3743)
Mouse anti-ADAR1 (1:500 dilution, Santa Cruz Bio, sc-73408)
Rabbit anti-actin (1:5,000 dilution, Cell Signaling, 4967)
Goat anti-rabbit secondary antibody, horseradish peroxidase -conjugated (1:5,000 dilution; Calbiochem, 401393)
Goat anti-mouse secondary antibody horseradish peroxidase-conjugated (1:5,000 dilution; Invitrogen, 31430)
Rabbit anti-ZBP1/DAI (1:1,000 dilution; Novus Biologicals NBP1-76854)
Rabbit anti-ISG15 (1:1000, Cell Signaling Technologies Cat # 2743)

Quantitative PCR. For qPCR analysis of mouse samples, RNA was extracted from mouse tissue using Trizol reagent (Ambion) according to manufacturer instructions. Reverse transcription PCR (RT-PCR) for cDNA synthesis was conducted using Maxima H Minus First Strand cDNA Synthesis Kit (Thermo Scientific) following manufacturer instructions. QPCR analysis for quantification of cellular transcripts was done using 2X qPCR Green Master Mix (APEX). For qPCR analysis from human cell lines, RNA extractions were done using an RNAeasy kit (Qiagen) according to kit protocol. RT- and qPCR were performed as described above. Transcripts were quantified using the $\Delta\Delta C_T$ method relative to *Gapdh* or β-Actin (*Actb*) transcripts.

Immunoblotting. Cells were homogenized in RIPA buffer and protein content was determined by Bradford reaction (Bio-Rad). 30 µg total protein was loaded per well prepared in 6X reducing SDS sample buffer (Bio-Rad, boil for 5-10 minutes prior to loading). Samples were run on 10% agarose gels (Bio-Rad) and transferred to polyvinylidene difluoride membrane (Bio-Rad). Samples were blocked in 5% milk in tris-buffered saline containing 0.1% Tween20 (TBS-T). Immobilon Crescendo Western HRP substrate (Millipore) was used for visualization of bands and imaged on a ChemiDoc XRS+ Imaging System (Bio-Rad).

Cell culture and siRNA delivery. Triplicate biological replicates were used with three technical replicates each. A549 cell lines (ATTC, CCL-185) were maintained in Dulbecco's Modified

Eagle's Medium (Corning) containing 10% fetal bovine serum and penicillin/streptomycin/L-glutamine (Corning, 100x solution). Doxycycline-inducible RdRp-expressing cells were described previously (1). Two different siRNAs were used in combination for *ADAR* knockdown and were purchased from ThermoFisher Scientific (Catalog # 4390824, IDs s1008, s1009, previously validated). Negative control (ThermoFisher) or anti-*ADAR* siRNA were transfected into cells (50 pmol per well in a 6-well plate, cells seeded at >50% confluence) using lipofectamine RNAimax reagent (ThermoFisher) according to manufacturer instructions. Cells were washed 6 hours post transfection and dox (2 µg/mL) was added at this time. At 48 hours post dox addition, cells were lysed for protein and RNA analysis.

Bioinformatics and Computational Methods. We used a combination of RNA sequencing and exome sequencing to evaluate transcriptome-wide patterns of RNA gene expression and ADAR-mediated A-to-I RNA editing. Specifically, we sequenced four biological replicates from each of the four genotypes for RNA-seq (WT-*Adar*$^{+/+}$, WT-*Adar*$^{+/-}$, *RdRp*$^{tg/-}$ *Adar*$^{+/+}$, and *RdRp*$^{tg/-}$*Adar*$^{+/-}$) and a single sample from each genotype for exome sequencing. Exome sequencing was used to establish a baseline level of germline genetic variation within our mouse colony and was used as background for identifying RNA-edited sites. Library preparation and sequencing for single-end RNA-sequencing and paired-end exome sequencing were performed by BGI (Beijing Genomics Institute). The quality of raw reads was assessed using FASTQC v.0.11.5. We used Trimmomatic v.0.27 to filter out low quality reads that had a mean Phred quality score less than 20. Read quality was then reassessed with FASTQC. We used Hisat2 v.2.1.0 to map reads to the mm10 genome using default single-end parameters for RNA-seq and included the --no-mixed --no-discordant flags for the paired-end exome sequencing. Next we used Samtools v.1.3.1 to convert the sam output files into bam format. Then we used PicardTools v.1.119 to add read groups, remove PCR duplicates, and coordinate sort the bam files. To evaluate RNA-seq gene expression patterns across the four genotypes, we first used Stringtie v.1.3.6 to quantify transcripts abundance, and Stringmerge to merge the output Stringtie GTF files. CuffDiff2 was to identify significantly differentially expressed genes (DEGs) with an FDR of 0.05 and Benjamini-Hochberg multiple test correction. In order to reduce false positives, we also required fragments per kilobase per million reads mapped (FPKM) to be at least four, and at 2-fold differences in expression because of the massive gene expression differences observed in(1, 2). We used CummeRbund and Plotly to visualize our results. The Interferome Database was used to identify which DEGs were known ISGs. Finally, we used the Canonical Pathways and Diseases and Biological Functions analyses in IPA to determine which molecular pathways and biological functions were enriched among our conditions and to predict whether they were likely to be activated or inhibited based on gene expression patterns in our dataset. To identify RNA-edited sites, we used REDItools to call SNPs that were present in the RNA-seq, but not present in the exome sequencing. Because the A-to-I editing performed by ADAR is incorporated as A-to-G changes by sequencers, we looked for differences in A-to-G changes across conditions. We required a minimum of 10x coverage and that each putative RNA-editing SNP be sequenced at least twice to reduce the risk of including sequencing errors. First, we used Samtools mpileup to call SNPs in the exome sequencing data. We used REDItoolsDeNovo to call SNPs A-to-I edited sites in the RNA-seq requiring at least 10x coverage and that each SNP was sequenced at least twice. Putative germline SNPs identified in the exome sequencing were subtracted from the RNA SNPs. The resulting SNP tables were converted into bed format and sorted by coordinates using BedTools and we filtered SNPs to those present in all four biological replicates. We then annotated the SNPs using Homer annotatePeaks.pl to determine the genomic features in which SNPs occur. A-to-I editing patterns were compared across the four genotypes in two ways and visualized using SUMO, 1) whether editing occurred in the same vs. different genomic features, allowing editing sites to occur at different locations within that feature, and 2) whether editing occurred at identical sites. Finally, we used IPA to identify significantly enriched molecular pathways and biological functions associated with edited genes

among the 4 genotypes. The RNA-seq and whole exome sequencing datasets have been deposited to the NCBI sequence read archive (SRA SUB14698103).

Flow Cytometry. Mice were euthanized by CO_2 asphyxiation and subsequent cardiac puncture. Spleens were excised and placed in 15 mL conical tubes containing 3 mL of DMEM containing FBS and antibiotics. Spleen was manually dissociated with a pipette tip and pipetting, then passed through a 40 µM nylon cell strainer. 100 µL from each sample were combined and used for the isotype and unstained controls. Cells were gated to exclude debris, doublets, and dead cells based on viability dye staining. Cell population abundance: samples had at least 1x10^6 cells sorted in the live population and cell types are shown as percent of live cells for all flow cytometry data. Each cell type described had a minimum of about 0.5% meaning all cell types described were observed at a frequency of about 5,000 or more per sample. Analysis of cellular populations was conducted as previously described (3). For staining of splenocyte populations, cells were red blood cell depleted as described (3). For analysis including FoxP3 staining, intracellular transcription factor staining was done using Foxp3/Transcription Factor Staining Buffer Set (eBioscience) according to manufacturer instructions for use in a 96-well plate. DC-specific staining panel has been previously described (3). T_{reg} staining panel consists of the following antibodies/cellular stains: fixable viability dye eFlour780 (eBioscience, 65-0865-14), PE anti-mouse FoxP3 (BioLegend, 126404), PerCP-Cy5.5 anti-mouse CD4 (BioLegend, 100434), Brilliant Violet 421 anti-mouse CD25 (BioLegend, 101923), APC anti-mouse CTLA-4 (BioLegend, 106310), Brilliant Violet 711 anti-mouse GITR (BD Bioscience, 563390), Brilliant Violet 605 anti-mouse ICOS (BioLegend, 313538), Brilliant Violet 480 anti-mouse CD44 (BD Bioscience, 566116) and FITC anti-mouse CD62L (BioLegend, 104406). For analysis of B cells (germinal center and plasmablast) the following antibodies and cellular stains were used: fixable viability dye eFlour780 (eBioscience, 65-0865-14), Brilliant Violet 421 anti-mouse CD138 (BioLegend, 142507), PE anti-mouse Fas (BD Bioscience, 554258), Alexa Fluor 488 anti-mouse GL-7 (BioLegend, 144612). For T_{FH} cell analysis and CD45.1 engraftment, the following antibodies and cellular stains were used: fixable viability dye eFlour780 (eBioscience, 65-0865-14), PerCP-Cy5.5 anti-mouse CD4 (BioLegend, 100434), Brilliant Violett 711 anti-mouse TCRβ (BioLegend, 109243), PE anti-mouse PD-1 (BioLegend, 135205), APC anti-mouse CXCR5 (BioLegend, 145506), and Brilliant Violet 421 anti-mouse CD45.1 (BioLegend, 110732). BST-2 was detected with Pacific Blue anti-mouse BST-2 (BioLegend, 127108). Gating for B cell and T_{FH} cell analysis was described in ref (4). Isotype staining for each panel was done in parallel. Gating was set based on fluorescence minus one controls. Cells were gated to exclude debris, doublets, and dead cells based on viability dye staining. Gating for DC-subtype determination was described in ref. (3). All data was acquired on an LSRII (BD Biosciences) and analysis was done using FlowJo software.

ELISAs. Mouse serum was used for ANA detection via ELISA. For detection of anti-dsDNA antibodies, calf thymus DNA (Sigma, D4522) was digested with S1 nuclease (ThermoFisher, EN0321) to remove any single stranded DNA (ssDNA). DNA was ethanol precipitated and resuspended in nuclease free water. Freeze-thaw cycles were avoided to prevent creation of new ssDNA. Nunc MaxiSorp ELISA plates (Sigma) were coated with Poly-L Lysine (0.01% final, Millipore Sigma) prior to use. Plates were coated overnight with dsDNA (3 µg/mL) in PBS at room temperature and blocked with BSA in PBS (3% final, Sigma). For a standard, anti-dsDNA (Abcam, ab27156) was used between the range of 1 µg/mL – 1.37 ng/mL (3-fold dilutions) and serum samples were initially diluted 1:10 and then as needed. For anti-smAg ELISAs, plates were coated with Sm Ag (3 µg/mL, Genway Biotech, GWB-CA4A65) in PBS overnight. Blocking was done in 1% BSA/PBS. For standard, anti-SmAg (Novus Biologicals, NB600-546) was used between the range of 1 µg/mL – 15.63 ng/mL (2-fold dilutions) and serum samples were diluted 1:10 before use and then as needed. For both ELISAs, standard and serum samples were diluted in sample buffer (0.5% Tween20, 1% BSA in PBS) and plates were washed 3-5 times between incubations with wash solution (0.5% Tween20 in PBS). Plates were incubated with samples/standard for 2 hours at 37°C. Detection antibody used was goat anti-mouse IgG

peroxidase (1:10,000 dilution; Sigma, A2554) and peroxidase was developed used TMB ELISA HRP Substrate kit (Seracare) and Sulfuric acid (4N, Fisher Scientific) according to manufacturer instructions.

Calcium Quantification. Whole-brain tissue was flash frozen at necropsy, homogenized by sonication on ice in 4x volumes of calcium assay buffer (Calcium Assay Kit, Abcam ab102505), and free Ca^{2+} ions were quantified following the manufacturer's methods.

Histopathology. Briefly, approximately 2 cm thick tissue sections of 5 week old mice were fixed in 10% formalin for 24 hours then washed twice and suspended in 70% ethanol. This age was chosen as by this point the mice already showed notable changes in growth but had not yet begun to succumb to disease related mortality. Tissues were paraffin embedded, cut and stained for Alizarin Red or H&E by our Research Histology Core Laboratory. H&E-stained slides were analyzed and scored by the IDEXX BioAnalytics histopathology group and are shown in the figure below. Grading was: 0 no change from WT, 1 minimal, 2 mild, 3 moderate, 4 marked changes. All scores were zero except for one $RdRp^{tg}$ kidney which was scored 1.

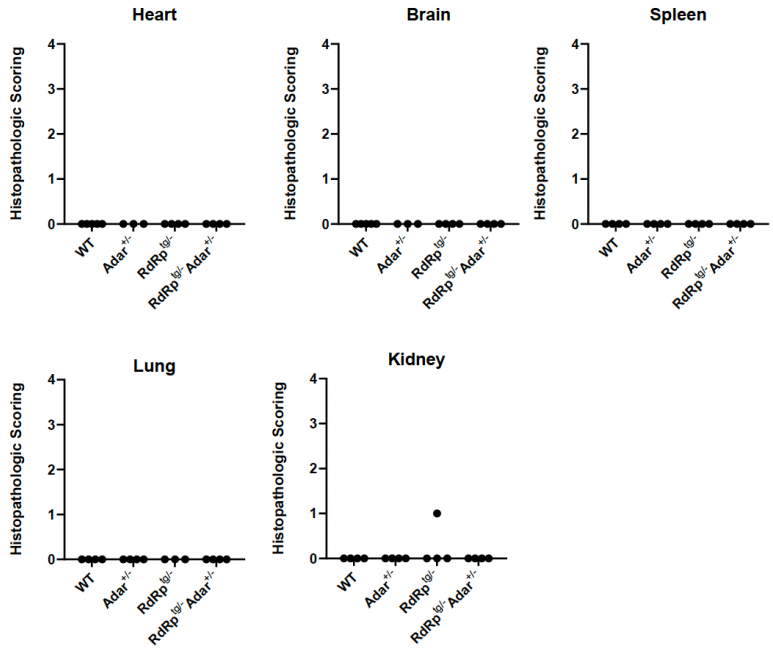

Figure. Histopathological grading of mouse tissues. No significant changes or differences were noted in the $RdRp^{tg/-}$ $Adar^{+/-}$ animals to explain the clinical presentations of this genotype.

References for Supplemental Methods

1. Painter MM, Morrison JH, Zoecklein LJ, Rinkoski TA, Watzlawik JO, Papke LM, et al. Antiviral Protection via RdRP-Mediated Stable Activation of Innate Immunity. *PLoS pathogens.* 2015;11(12):e1005311.
2. Bankers L, Miller C, Liu G, Thongkittidilok C, Morrison J, and Poeschla EM. Development of interferon-stimulated gene expression from embryogenesis through adulthood, with and without constitutive MDA5 pathway activation. *Journal of Immunology.* 2020;204(10):2791-807.
3. Miller CM, Barrett BS, Chen J, Morrison JH, Radomile C, Santiago ML, et al. Systemic Expression of a Viral RdRP Protects against Retrovirus Infection and Disease. *Journal of virology.* 2020;94(9).
4. Klarquist J, and Janssen EM. The bm12 Inducible Model of Systemic Lupus Erythematosus (SLE) in C57BL/6 Mice. *J Vis Exp.* 2015(105):e53319.